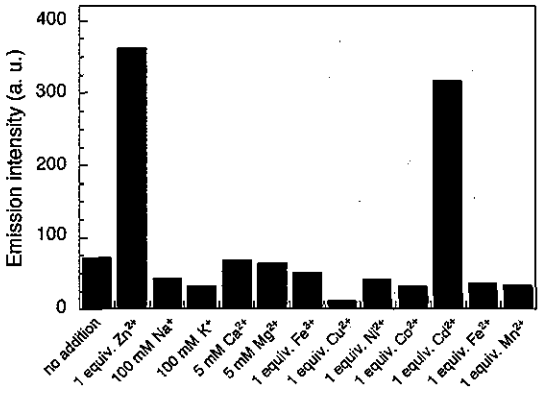

Figure 5. Luminescence intensity change profiles of **[Eu-7]** (50 μM) in the presence of various cations in 100 mM HEPES buffer at pH 7.4, 22 °C (excitation 320 nm, emission 614 nm). Heavy metal ions (1 equiv relative to **[Eu-7]**) were added as $Fe_2(SO_4)_3$, $CuSO_4$, $NiSO_4$, $CoSO_4$, $CdSO_4$, $FeSO_4$, and $MnSO_4$. Other cations were added as $ZnSO_4$ (50 μM), $NaNO_3$ (100 mM), KNO_3 (100 mM), $CaCl_2$ (5 mM), and $MgSO_4$ (5 mM).

[Eu-7] (50 μM) was not observed upon the addition of 100 mM Na^+ or K^+, 5 mM Ca^{2+} or Mg^{2+}, or 50 μM of various heavy metal ions except for Cd^{2+} (Figure 5). Thus, Na^+, K^+, Ca^{2+}, and Mg^{2+}, which exist at high concentrations in biological systems, did not enhance the luminescence intensity of **[Eu-7]**. The luminescence emission intensity was weakened or quenched upon the addition of several cations (particularly Cu^{2+}, Ni^{2+}, and Co^{2+}) together with Zn^{2+}, in comparison with that upon adding Zn^{2+} alone, as shown in Figure S8. However, Zn^{2+} can be distinguished from these heavy metals, since Zn^{2+} chelation selectively enhances the luminescence intensity.

Utility of the Long-Lived Luminescence. To explore further the utility of the long luminescence lifetime of **[Eu-7]**, we tested whether it could be well distinguished from the short-lived background fluorescence and scattered light. Figure 6 presents the emission spectra of **[Eu-7]** solution, with 1 μM rhodamine 6G as an artificial short-lived background, without (Figure 6a) or with (Figure 6b) a time resolution process. There are three fluorescent peaks in Figure 6a due to scattered light (300 nm), the increased fluorescence of the quinoline moiety (around 400 nm), and the fluorescence of rhodamine 6G (around 550 nm). Among them, rhodamine 6G fluorescence can directly interfere with Eu^{3+} luminescence. However, the long-lived luminescence detection of **[Eu-7]** solution was not affected at all by these three peaks (Figure 6b). Thus, the luminescence of **[Eu-7]** should be little influenced by experimental artifacts when measured with the aid of a time-resolution process.

Biological Applications of [Eu-7]. We next examined the application of **[Eu-7]** to cultured living cells (HeLa cells) by fluorescence microscopy (Figure 7). Since **[Eu-7]** can be excited with a relatively long excitation wavelength, this compound is suitable for cellular applications, in contrast to previously reported Zn^{2+}-sensitive luminescent lanthanide sensors. The fluorescence microscope had an optical window centered at 617 ± 37 nm for the emission due to Eu^{3+}-based luminescence upon excitation at 360 ± 40 nm (the Stoke's shift is >250 nm). Compound **[Eu-7]** was injected only into the single cultured HeLa cell in the bottom left-hand part of the field of view in Figure 7. We then added Zn^{2+} (150 μM) and a zinc-selective ionophore, pyrithione (2-mercaptopyridine *N*-oxide, 50 μM), to the medium at 3 min, inducing a prompt increase of intracellular luminescence. This luminescence was decreased by extracellular

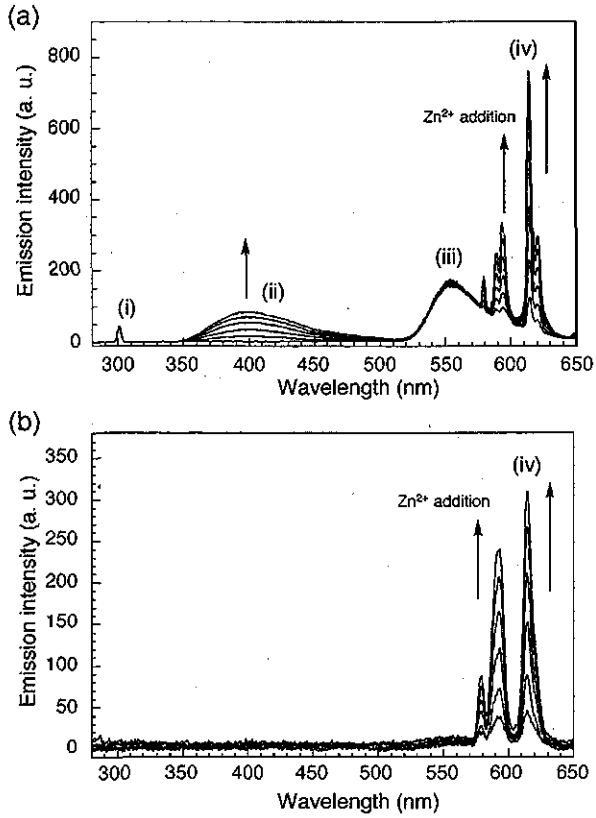

Figure 6. Emission spectra of **[Eu-7]** (50 μM) without (a) and with (b) time resolution in the presence of various concentrations of Zn^{2+}: 0, 0.2, 0.4, 0.6, 0.8, and 1.0 equiv of Zn^{2+} with respect to **[Eu-7]** (excitation at 300 nm, respectively). Both spectra were measured in 100 mM HEPES buffer containing 1 μM rhodamine 6G as a chromophore to provide artificial background fluorescence at pH 7.4 and 22 °C. The emission spectra (a) were measured with a Hitachi F4500, and the time-resolved emission spectra (b) were measured using a delay time of 0.05 ms and a gate time of 1.00 ms with a Perkin-Elmer LS-50B. Bands can be assigned to (i) scattered excitation light, (ii) the fluorescence of the quinolyl chromophore of **[Eu-7]**, (iii) the fluorescence of rhodamine 6G, and (iv) the long-lived luminescence of **[Eu-7]**.

addition of the cell-membrane-permeable chelator TPEN (150 μM) at 7.5 min. Clear images were obtained, because **[Eu-7]** has long-wavelength emission with a large Stoke's shift, which minimizes the influence of the excitation light. These results demonstrate that **[Eu-7]** can be used to monitor changes of intracellular ionic Zn^{2+} reversibly, and has potential for biological applications.

Conclusions

We have designed and synthesized a novel lanthanide-based luminescent sensor molecule for Zn^{2+}, **[Eu-7]**, by using Eu^{3+} as the fluorophore and a quinolyl moiety as the antenna. This compound **[Eu-7]** showed pronounced long-lived luminescence enhancement upon Zn^{2+} addition. Previously reported Zn^{2+}-sensitive lanthanide sensors are not suitable for biological applications, because of their short excitation wavelength, small enhancement of emission, inconvenient pH sensitivity, etc. In contrast, the properties with **[Eu-7]** are favorable for biological applications. It is noteworthy that **[Eu-7]** has a longer excitation wavelength than previously reported Zn^{2+}-sensitive lanthanide sensors, and this permits fluorescence microscopy measurements with **[Eu-7]** to monitor Zn^{2+} concentrations in living cells. We expect that a larger signal-to-noise ratio in cellular imaging

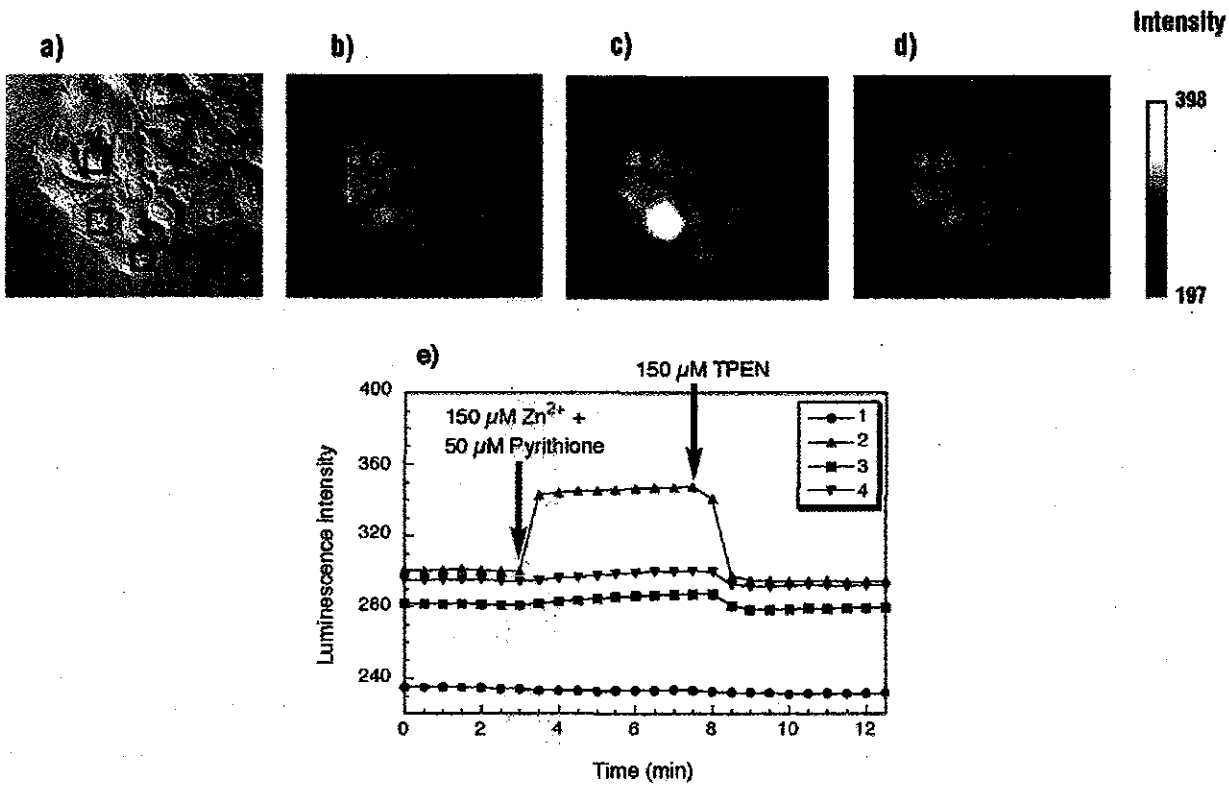

Figure 7. Bright-field transmission and luminescence images of Zn^{2+} in **[Eu-7]**-injected HeLa cells in HBSS buffer. The luminescence at 580−654 nm, excited at 320−400 nm, was measured at 30 s intervals. The cells were cultured in DMEM supplemented with 10% fetal bovine serum, 1% penicillin, and 1% streptomycin at 37 °C in a 5% CO_2/95% air incubator. The cells were then washed with HBSS buffer and injected with **[Eu-7]** solution. (a) Bright-field transmission image (0 min). (b) Luminescence image of (a) (0 min). (c) Luminescence image (5 min) following an addition of 50 μM pyrithione (zinc ionophore) and 150 μM $ZnSO_4$ to the medium at 3 min. (d) Luminescence image (10 min) following an addition of 150 μM TPEN to the medium at 7.5 min. Luminescence images (b−d) correspond to the luminescence intensity data in (e), which shows the average intensity of the corresponding area or cell area (1, extracellular region; 2, intracellular region of the injected cell; 3, 4, intracellular regions of noninjected cells).

would be achievable by using time-resolved imaging with **[Eu-7]**. Furthermore, we confirmed the advantage of the long-lived luminescence of **[Eu-7]** for eliminating fluorescence background interference. This complex **[Eu-7]** is the first Zn^{2+}-sensitive luminescent lanthanide chemosensor that can be used for studies on the biological functions of Zn^{2+}, and our design strategy should yield a range of long-lived luminescent lanthanide probes for sensing Zn^{2+} or, after appropriate modification of the acceptor moiety, other molecules of interest in biological applications.

Experimental Section

Materials. DTPA bisanhydride was purchased from Aldrich Chemical Co. Inc. (St. Louis, MO). All other reagents were purchased from either Tokyo Kasei Kogyo Co., Ltd. (Japan) or Wako Pure Chemical Industries, Ltd. (Japan). All solvents were used after distillation. Silica gel column chromatography was performed using BW-300, Chromatorex-NH, and Chromatorex-ODS (all from Fuji Silysia Chemical Ltd.).

Instruments. ^1H and ^{13}C NMR spectra were recorded on a JEOL JNM-LA300. Mass spectra were measured with a JEOL JMS-DX 300 mass spectrometer (EI^+) or a JEOL JMS-700 mass spectrometer (FAB^+). HPLC purification was performed on a reverse-phase column (GL Sciences (Tokyo, Japan), Inertsil Prep-ODS 30 mm × 250 mm) fitted on a Jasco PU-1587 System. Time-resolved fluorescence spectra were recorded on a Perkin-Elmer LS-50B (Beaconsfield, Buckinghamshire, England). The slit width was 5 nm for both excitation and emission. UV−visible spectra were obtained on a Shimadzu UV-1600 (Tokyo, Japan). Fluorescence spectroscopic studies were performed with a Hitachi F4500 (Tokyo, Japan). The slit width was 2.5 nm for both excitation and emission. The photomultiplier voltage was 700 V. Measurements of relaxation times T_1 were made using an NMR analyzer operating at 20 MHz (Minispec mq20, Bruker).

Time-Delayed Luminescence Spectral Measurements. The time-delayed luminescence spectra of **[Eu-7]** (50 μM) were measured in 100 mM HEPES buffer at pH 7.4, 22 °C (excitation at 320 nm), with addition of various amounts of Zn^{2+} (0, 0.1, 0.2, 0.3, 0.4, 0.5, 0.6, 0.7, 0.8, 0.9, 1.0, 1.1, 1.2, 2.0, 3.0, 4.0, 5.0, and 10.0 equiv of Zn^{2+}) to **[Eu-7]**. The slit width was 5 nm for both excitation and emission. A delay time of 0.05 ms and a gate time of 1.00 ms were used.

UV−Visible Absorption Spectral Measurements. The absorption spectral changes of **[Eu-7]** (50 μM) upon addition of Zn^{2+} were measured at 22 °C in an aqueous solution buffered to pH 7.4 (100 mM HEPES buffer). Zn^{2+} was added as $ZnSO_4$ at 0, 0.2, 0.4, 0.6, 0.8, 1.0, 2.0, 3.0, 4.0, 5.0, and 10.0 equiv of Zn^{2+} with respect to **[Eu-7]**.

Fluorescence Emission Spectral Measurements. The fluorescence emission spectra of **[Eu-7]** (20 μM) without a delay time were measured in 100 mM HEPES buffer (pH 7.4) at 22 °C, following excitation at 320 nm. The amounts of added Zn^{2+} were 0, 0.2, 0.4, 0.6, 0.8, 1.0, 2.0, 3.0, 4.0, 5.0, and 10.0 equiv with respect to **[Eu-7]**.

Quantum Yield Measurements. The luminescence spectra were measured with a Hitachi F4500 spectrofluorometer. The slit width was 2.5 nm for both excitation and emission. The photomultiplier voltage was 950 V. The luminescence spectra of **[Eu-7]** were measured in 100 mM HEPES buffer at pH 7.4, 25 °C, with irradiation at 300 nm. The quantum yields of Eu^{3+} complexes were evaluated using a relative method with reference to a luminescence standard, $[Ru(bpy)_3]Cl_2$ (ϕ = 0.028 in air-equilibrated water).[29] The quantum yields of Eu^{3+} complexes can be expressed by eq 2,[30] where Φ is the quantum yield (subscript "st" stands for the reference and "x" for the sample), A is

(29) Nakamura, K. *Bull. Chem. Soc. Jpn.* **1982**, *55*, 2697−2705.

$$\Phi_x/\Phi_{st} = [A_{st}/A_x]\,[n_x^2/n_{st}^2]\,[D_x/D_{st}] \quad (2)$$

the absorbance at the excitation wavelength, n is the refractive index, and D is the area (on an energy scale) of the luminescence spectra. The samples and the reference were excited at the same wavelength. The sample absorbance at the excitation wavelength was kept as low as possible to avoid fluorescence errors ($A_{exc} < 0.06$).

Luminescence Lifetime Measurements. The luminescence lifetimes of the complexes were recorded on a Perkin-Elmer LS-50B. The data were collected with 10-μs resolution in H_2O (100 mM HEPES buffer at pH 7.4) and D_2O (100 mM HEPES buffer at pD 7.4, based on the equation pD = pH + 0.40[31]), and fitted to a single-exponential curve obeying eq 3, where I_0 and I are the luminescence intensities at the

$$I = I_0 \exp(-t/\tau) \quad (3)$$

time $t = 0$ and time t, respectively, and τ is the luminescence emission lifetime. Lifetimes were obtained by monitoring the emission intensity at 614 nm (λ_{ex} = 320 nm).

Relaxation Time Measurements. The relaxation time, T_1, of aqueous solutions of the Gd^{3+} complex **[Gd-7]** was measured in 100 mM HEPES buffer (pH 7.4) at 20 MHz and 25 °C (Minispec mq20, Bruker). The value of T_1 was measured from 10 data points generated by using the standard inversion–recovery procedure. The relaxivity, R_1 ($mM^{-1}\ s^{-1}$), of **[Gd-7]** was determined from the slope of the plot of $1/T_1$ vs [**[Gd-7]**] (0, 0.4, 0.6, 0.8, and 1.0 mM). The buffered Gd^{3+} complex (**[Gd-7]**) solution was allowed to equilibrate for at least 10 min after addition of $ZnSO_4$ aqueous stock solution.

Apparent Dissociation Constant (K_d) Measurements. Upon addition of various concentrations of Zn^{2+}, the luminescence intensity and the absorbance of **[Eu-7]** linearly changed up to a 1:1 [Zn^{2+}]/[**[Eu-7]**] molar ratio, and the luminescence and absorption spectra remained at a plateau with further addition of Zn^{2+}. Furthermore, the Job's plot analysis revealed that maximum luminescence intensity was obtained at a 1:1 ratio. These data suggested that **[Eu-7]** should form a 1:1 complex with Zn^{2+}. So, the apparent dissociation constant, K_d, was determined from the luminescence intensity in 100 mM HEPES buffer (pH 7.4, I = 0.1 ($NaNO_3$)) at 22 °C (λ_{exc} = 320 nm). [Zn^{2+}] was controlled by using 0–9 mM $ZnSO_4$/10 mM NTA (nitrilotriacetic acid) systems[19b,32] below 398 nM free Zn^{2+} and unbuffered Zn^{2+} above 200 μM free Zn^{2+}. The luminescence intensity data were fitted to eq 4, and K_d was calculated, where F is the luminescence intensity, F_{max}

$$F = F_0 + (F_{max} - F_0)\,([Zn^{2+}]_f)/(K_d + [Zn^{2+}]_f) \quad (4)$$

is the maximum luminescence intensity, F_0 is the luminescence intensity with no addition of Zn^{2+}, and $[Zn^{2+}]_f$ is the free Zn^{2+} concentration. The value of K_d was determined from the fittings for the luminescence intensity data shown in the Supporting Information.

Phosphorescence Spectral Measurements. Phosphorescence spectra were obtained with a Hitachi F4500. The phosphorescence spectra of **[Gd-7]** (20 μM) in the absence and in the presence of Zn^{2+} (1 equiv relative to **[Gd-7]**) were measured at 77 K in MeOH:EtOH = 1:1 (excitation at 320 nm) (see Supporting Information). The slit width was 10.0 nm for excitation and 20.0 nm for emission. The photomultiplier voltage was 950 V.

Effect of pH on the Luminescence Intensity. The following buffers were used: 100 mM $ClCH_2COOH$–$ClCH_2COONa$ buffer (pH 3.6), 100 mM AcOH–AcONa buffer (pH 4.0–5.5), 100 mM morpholinoethanesulfonic acid (MES) buffer (pH 5.5–6.5), 100 mM HEPES buffer (pH 7.0–8.0), and 100 mM *N*-cyclohexyl-2-aminoethanesulfonic acid (CHES) buffer (pH 8.5–9.0). The luminescence intensity (excitation 320 nm, emission 614 nm) of each sample of **[Eu-7]** (50 μM) was plotted.

Metal Ion Selectivity Measurements. The luminescence emission enhancement of **[Eu-7]** was measured in 100 mM HEPES buffer (pH 7.4) at 22 °C (excitation 320 nm, emission 614 nm). Heavy metal ions (50 μM) were added as $Fe_2(SO_4)_3$, $CuSO_4$, $NiSO_4$, $CoSO_4$, $CdSO_4$, $FeSO_4$, and $MnSO_4$. Other cations were added as $ZnSO_4$ (50 μM), $NaNO_3$ (100 mM), KNO_3 (100 mM), $CaCl_2$ (5 mM), and $MgSO_4$ (5 mM).

Confirmation of the Utility of the Long Luminescence Lifetime of [Eu-7]. The emission spectra without a time-resolution process were measured with a Hitachi F4500. The time-resolved emission spectra were measured with a Perkin-Elmer LS-50B using a delay time of 0.05 ms and a gate time of 1.00 ms. Spectra of **[Eu-7]** (50 μM) with various concentrations of Zn^{2+} were measured in 100 mM HEPES buffer (pH 7.4) at 22 °C containing 1 μM rhodamine 6G as an artificial provider of short-lived background fluorescence (excitation at 300 nm). The amounts of added Zn^{2+} were 0, 0.2, 0.4, 0.6, 0.8, and 1.0 equiv of Zn^{2+} with respect to **[Eu-7]**.

Preparation of Cells. HeLa cells were cultured in Dulbecco's modified Eagle's medium (DMEM) (Invitrogen Corp., Carlsbad, CA), supplemented with 10% fetal bovine serum (Invitrogen Corp.), 1% penicillin, and 1% streptomycin (Invitrogen Corp.) at 37 °C in a 5% CO_2/95% air incubator. The cells were grown on an uncoated 35-mm-diameter glass-bottomed dish (MatTek, Ashland, MA), and washed twice with Hanks' balanced salt solution (HBSS) buffer (Invitrogen Corp.), and then the medium was replaced with HBSS buffer before imaging. The compound **[Eu-7]** (2 mM) was dissolved in microinjection buffer (HBSS buffer), and injected into the cells with an Eppendorf injection system (Transjector 5246).

Microscopy and Imaging Methods. The imaging system comprised an inverted microscope (IX71; Olympus) and a cooled CCD camera (Cool Snap HQ; Roper Scientific, Tucson, AZ). The microscope was equipped with a xenon lamp (AH2-RX; Olympus), a 40× objective lens (Uapo/340, N.A. 1.35; Olympus), a dichroic mirror (420DCLP; OMEGA), an excitation filter (S360/40×; Chroma), and an emission filter (S617/73m; Chroma). The whole system was controlled using MetaFluor 6.1 software (Universal Imaging, Media, PA). The luminescence images were measured every 30 s. Additions of zinc sulfate (150 μM) with pyrithione (50 μM) or *N,N,N′,N′*-tetra(2-picolyl)-ethylenediamine (TPEN) (150 μM) to cell samples were performed on the microscope stage.

Acknowledgment. This work was supported in part by the Ministry of Education, Culture, Sports, Science and Technology of Japan (Grants for The Advanced and Innovational Research Program in Life Sciences to T.N., 15681012 and 16048206 to K.K.). K.K. was also supported by the Sankyo Foundation, by the Kanagawa Academy of Science, and by the Suzuken Memorial Foundation. K.H. is the recipient of Research Fellowships of the Japan Society for the Promotion of Science for Young Scientists.

Supporting Information Available: Detailed descriptions of synthetic procedures for **[Eu-7]** and **[Gd-7]**; data on the measurements of the emission lifetime of **[Eu-7]** and on the measurement of the apparent dissociation constant of **[Eu-7]** with Zn^{2+}; phosphorescence spectra of **[Eu-7]**; plot of the absorbance intensity changes detected at 340 nm, shown in Figure 3; Job's plot for complexation between **[Eu-7]** and Zn^{2+}; plot of the changes in the fluorescence intensity detected at 397 and 614 nm, shown in Figure 4; and pH profile of the luminescence intensity of **[Eu-7]**. This material is available free of charge via the Internet at http://pubs.acs.org.

JA0469333

(30) Chen, Q. Y.; Feng, C. J.; Luo, Q. H.; Duan, C. Y.; Yu, X. S.; Liu, D. J. *Eur. J. Inorg. Chem.* **2001**, 1063–1069.
(31) Wang, Y. M.; Wang, Y. J.; Wu, Y. L. *Polyhedron* **1998**, *18*, 109–117.
(32) Hirano, T.; Kikuchi, K.; Urano, Y.; Higuchi, T.; Nagano, T. *J. Am. Chem. Soc.* **2000**, *122*, 12399–12400.

J|A|C|S
ARTICLES
Published on Web 06/15/2004

Nonspecific Medium Effects versus Specific Group Positioning in the Antibody and Albumin Catalysis of the Base-Promoted Ring-Opening Reactions of Benzisoxazoles

Yunfeng Hu,† K. N. Houk,*,† Kazuya Kikuchi,‡ Kinya Hotta,‡ and Donald Hilvert*,‡

Contribution from the Department of Chemistry and Biochemistry, University of California, Los Angeles, Los Angeles, California 90095-1569 and Department of Chemistry, Scripps Research Institute, La Jolla, California 92037, and Laboratorium für Organische Chemie, Swiss Federal Institute of Technology, ETH–Hönggerberg, CH-8093, Zürich, Switzerland

Received February 18, 2004; E-mail: houk@chem.ucla.edu; hilvert@org.chem.ethz.ch

Abstract: The mechanisms by which solvents, antibodies, and albumins influence the rates of base-catalyzed reactions of benzisoxazoles have been explored theoretically. New experimental data on substituent effects and rates of reactions in several solvents, in an antibody, and in an albumin are reported. Quantum mechanical calculations were carried out for the reactions in water and acetonitrile, and docking of the transition state into a homology model of antibody 34E4 and an X-ray structure of human serum albumin was accomplished. A microenvironment made up of catalytic polar groups (glutamate in antibody 34E4 and lysine in human serum albumin) surrounded by relatively nonpolar groups is present in both catalytic proteins.

Introduction

The conversions of benzisoxazoles to cyanophenoxides with bases and various catalysts, often referred as the "Kemp elimination,"[1a–b] have been used as a probe of medium effects on the rates of reactions (Figure 1). The rates of these reactions are very sensitive to solvent polarity. Kemp and co-workers' classic studies of the effect of substituents and solvents established that the acetate-promoted reaction of 5-nitrobenzisoxazole is 10^8 times faster in acetonitrile than water.[1c–d] This reaction has subsequently been shown to be catalyzed by catalytic antibodies ($k_{cat}/k_{uncat} = 10^6$),[2] serum albumins (10^3),[3–5] orphan antibodies (10^3),[6] a polyamine organic host (10^3),[7] surfactant vesicles (850),[8] micelles (400),[8] polyethyleneimine "synzymes" (10^5 per site),[9] and even coal (200).[10] Because

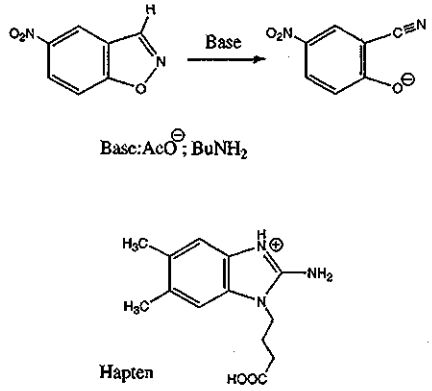

Figure 1. Base-catalyzed decomposition of benzisoxazoles (the "Kemp elimination") and the hapten used to elicit antibody 34E4.

different authors use different definitions for k_{cat} and k_{uncat}, those accelerations are not always directly comparable. For example, k_{uncat} can be considered as a pseudo-first-order rate constant of a water catalyzed reaction, or a second-order rate constant of an acetate or amine base-promoted reaction in water, whereas k_{cat} can be either a second-order rate constant in base-promoted reactions in different solvents or a first-order rate constant when saturated protein catalysts are involved. The various rate constants in different catalytic systems and the k_{uncat} used to compute them are listed in Table 1. The magnitude of the rate acceleration clearly depends on the pK_a of the base responsible for deprotonation and hence on the pH of the reaction medium. Catalysts such as antibody 34E4 and the polyethyleneimine "synzymes" exhibit high rate accelerations at pH values near their pK_a (ca. 6), whereas catalysts such as BSA with higher pK_a's (ca. 10) must contend with the high background rate at

† University of California, Los Angeles.
‡ Scripps Rsearch Institute and Swiss Federal Institute of Technology.

(1) (a) Casey, M. L.; Kemp, D. S.; Paul, K. G.; Cox, D. D. *J. Org. Chem.* **1973**, *38*, 2294–2301. (b) Kemp, D. S.; Casey, M. L. *J. Am. Chem. Soc.* **1973**, *95*, 6670–6680. (c) Kemp, D. S.; Paul, K. *J. Am. Chem. Soc.* **1975**, *97*, 7305–7312. (d) Kemp, D. S.; Cox, D. D.; Paul, K. *J. Am. Chem. Soc.* **1975**, *97*, 7312–7318.
(2) Thorn, S. N.; Daniels, R. G.; Auditor, M.-T. M.; Hilvert, D. *Nature* **1995**, *373*, 228–230.
(3) Hollfelder, F.; Kirby, A. J.; Tawfik, D. S. *Nature* **1996**, *383*, 60–63.
(4) Kikuchi, K.; Thorn, S. N.; Hilvert, D *J. Am. Chem. Soc.* **1996**, *118*, 8184–8185.
(5) Hollfelder, F.; Kirby, A. J.; Tawfik, D. S.; Kikuchi, K.; Hilvert, D. *J. Am. Chem. Soc.* **2000**, *122*, 1022–1029.
(6) Genre-Grandpierre, A.; Tellier, C.; Loirat, M. J.; Blanchard, D.; Hodgson, D. R. W.; Hollfelder, F.; Kirby, A. J. *Bioorg. Med. Chem. Lett.* **1997**, *7*, 2497–2502.
(7) Kennan, A. J.; Whitlock, H. W. *J. Am. Chem. Soc.* **1996**, *118*, 3027–3028.
(8) Perez-Juste, J.; Hollfelder, F.; Kirby, A. J.; Engberts, J. B. F. N. *Org. Lett.* **2000**, *2*, 127–130.
(9) Hollfelder, F.; Kirby, A. J.; Tawfik, D. S. *J. Org. Chem.* **2001**, *66*, 5866–5874.
(10) Shulman, H.; Keinan, E. *Org. Lett.* **2000**, *2*, 3747–3750.

10.1021/ja0490727 CCC: $27.50

Table 1. Rate Constants for the Uncatalyzed and Catalyzed Decarboxylations of 5-Nitrobenzisoxazoles in Different Catalytic Systems

catalyst	$k_{background}$ (s^{-1})[j]	k_{cat} (s^{-1})
34E4[a]	3.1×10^{-5}	0.66
34E4[b]	2.2×10^{-7}	0.30
BSA[c]	1.6×10^{-3}	2.5
BSA[d]	3.1×10^{-5}	0.017
orphan antibody 4B2[e]	$>3.1 \times 10^{-5}$	0.035
organic host[f]	1.1×10^{-7}	0.00063
coal[g]	6.8×10^{-5}	0.014
synzyme[h]	8.0×10^{-8}	0.045
Bu_4NOAc[i]	1.4×10^{-4} M^{-1}	
Et_3N[i]	8.2×10^{-1} M^{-1}	

[a] 20 °C, 40 mM phosphate buffer containing 100 mM NaCl, pH 7.4, ref 2. [b] 20 °C, 40 mM sodium acetate buffer containing 100 mM NaCl, pH 6.0 (the pK_a of the active site carboxylic acid), ref 2 and this work. [c] 20 °C, 40 mM sodium carbonate buffer containing 100mM NaCl, pH 10.2 (the pK_a of the active site amine), ref 4 and this work. [d] 20 °C, 40 mM phosphate buffer containing 100 mM NaCl, pH 7.4, Reference 4. [e] 30 °C, 1% CH_3CN, 40 mM phosphate buffer containing 100 mM NaCl, pH 7.1, ref 6. The value of $k_{background}$ originally reported in ref 6 is 1.9×10^{-6} s^{-1}, which is inconsistently low and is presumably a misprint. [f] Room temperature, $CDCl_3$, ref 7. [g] 4 °C, 50 mM phosphate buffer containing 2% acetonitrile, pH 7.4, ref 10. [h] 25 °C, 70 mM BisTris buffer, pH 5.9, ref 9. [i] 25° C, H_2O, ref 1d. [j] $k_{background}$ is obtained by extrapolation to zero buffer concentration.

high pH and are less efficient even though the absolute value of k_{cat} in the pH-independent range is higher.

Although many different interpretations have been offered for the catalysis by these diverse materials, the binding of substrate into a relatively nonpolar environment and particularly the desolvation of acetate have usually been thought to be responsible for the rate acceleration. By contrast, the amine-catalyzed reaction is relatively insensitive to solvent polarity, presumably because the uncharged base is not dramatically stabilized by hydrogen bonding. Thus, the reactions involving amine bases, such as polyamines, serum albumins, and synzymes are not easy to explain by medium polarity effects.

Vigorous discussion has broken out about how two types of protein catalysts, (1) tailored catalytic antibodies such as 34E4,[2] and (2) "off-the-shelf" proteins such as serum albumins,[3,4] accelerate this transformation. The two proteins are likely to exploit carboxylate and amine groups as catalytic bases, respectively. Hilvert and Kirby independently determined that serum albumins catalyze the Kemp ring-opening with k_{cat} similar to that found with catalytic antibody 34E4.[3,4] Hilvert identified Lys222 as the catalytic group in bovine serum albumin subdomain II A. There is also a set of positively charged residues that stabilize the phenolate product formed in the reaction.[4] However, Kirby proposed that the low polarity of the interiors of the albumin and 34E4 is the factor responsible for most of the rate acceleration in both cases.[3]

We have studied how these different proteins accelerate this reaction. Kinetic measurements on substituted compounds have been performed to show how specific interactions with nonpolar residues and nonspecific medium effects influence the stability and structure of the transition state. Quantum mechanical calculations of acetate and amine catalyzed reactions in the gas phase and in nonpolar and aqueous solutions have been used to explore the origins of acceleration by nonpolar solvents. The docking and binding of reactants and transition states in the antibody and serum albumin have provided detailed pictures of the origins of antibody and protein catalysis, specifically relative importance to catalysis of polarity and positioning of functional groups in the binding site.

Whether or not proteins can accelerate reactions merely by altering the microenvironment around a substrate and transition state has been the subject of an ongoing debate. Dewar attributed catalysis of chymotrypsin and carboxypeptidase A to the ability of these enzymes to eliminate solvent from the binding pocket and to provide a nonpolar environment for the reaction.[11] He also emphasized the importance of a nonpolar environment for acceleration of various reaction types.[12] On the other hand, Warshel has used thermodynamic arguments to show that desolvation effects alone are unlikely to be the origin of enzyme activity.[13] Although a polar molecule is destabilized by being bound into a nonpolar environment, a free energy penalty must be paid to remove the ionic molecule from water. Warshel proposes that electrostatic interactions between the oriented dipoles of the preorganized protein binding pocket and the substrate generally cause catalysis.[13] In general, Warshel embraces the effectively high polarity of protein binding sites and attributes catalysis to the ideal electrostatic complementarity of protein binding site and transition state.

Although some investigators have advocated pure medium effects ("The medium is the message" in McLuhan's words),[3] others have highlighted contributions of structural effects and specific interactions to catalysis. For example, Bruice emphasizes the ability of a protein to assemble substrates specifically into a geometry suitable for reaction (NACs, near attack conformations) regardless of the polarity of the microenvironment.[14]

Throughout these discussions, confusion has occasionally arisen by the use of different definitions of "medium." The dictionary definition emphasizes more or less homogeneous surroundings: "Any intervening substance through which a force acts on objects at a distance or through which impressions are conveyed to the senses: applied, e.g., to the air, the ether, or any substance considered with regard to its properties as a vehicle of light or sound."[15] This definition of "medium" implies a homogeneous environment. However, the word is often used to indicate specific characteristics of surroundings even when they are heterogeneous. "Microenvironment" is used here as a term to describe the active site of a protein catalyst, especially to convey the heterogeneity that is always a characteristic of a protein interior.

Kinetic Studies. Kemp explored the kinetics of the reactions of substituted benzisoxazoles (BI) with tertiary amines in water.[1] The kinetics follow Brønsted linear free energy relationships (LFERs) over a broad range of reactivity. The slope, β, of a plot of log k vs pK_a of the leaving group, pK_{lg}, provides a measurement of the relationship between the reaction rate and the reaction exothermicity and yields information about the structure and solvation of the transition state (TS).[16] We have measured the rates and β_{lg} values for these eliminations in several solvents and with protein catalysts. These are compared to water as a standard. Table 2 lists the benzisoxazoles studied,

(11) Dewar, M. J. S.; Storch, D. M. *Proc. Natl. Acad. Sci. U.S.A.* **1985**, *82*, 2225–2229.
(12) Dewar, M. J. S.; Healy, E. *Organometallics* **1982**, *1*, 1705–1708.
(13) Warshel, A. *J. Biol. Chem.* **1998**, *273*, 27035–29038.
(14) Bruice, T. C.; Lightstone, F. C. *Acc. Chem. Res.* **1999**, *32*, 127–136.
(15) Oxford English Dictionary, Second Edition, 1989.
(16) Hammond, G. S. *J. Am. Chem. Soc.* **1955**, *77*, 334–338; Leffler, J. E. *Science* **1953**, *117*, 340–341.

Table 2. Kinetic Parameters for the Decomposition of Substituted Benzisoxazoles

benzisoxazole	pK_a phenol	k_{AcO^-,H_2O} ($M^{-1}\,s^{-1}$)	k_{AcO^-,CH_3CN} ($M^{-1}\,s^{-1}$)	k_{BuNH_2,H_2O} ($M^{-1}\,s^{-1}$)	k_{BuNH_2,CH_3CN} ($M^{-1}\,s^{-1}$)	$(k_{cat}/K_m)_{34E4}$ ($M^{-1}\,s^{-1}$)	$(k_{cat}/K_m)_{BSA}$ ($M^{-1}\,s^{-1}$)
5,7-$(NO_2)_2$	0.6	2.76×10^{-3}	759 000			650 000	4530
5,6-$(NO_2)_2$	2.5	1.88×10^{-4}	57 800			3840	457
5-NO_2, 6-Cl	3.6	2.73×10^{-5}	4510	0.116	0.949	22 600	147
5-NO_2	4.1	1.33×10^{-5}	1000	0.0326	0.261	5450	23.9
5-CN	4.7	4.52×10^{-6}		0.0218	0.0603	144	1.81
6-NO_2	5.2	2.47×10^{-6}	104	0.0112	0.0247	0.177	1.52
5,6-Cl_2	5.6	1.52×10^{-6}		0.00854	0.0205	9.64	1.78
6-Cl	6.1		19.4			0.635	0.255
5-Cl	6.4					3.3	0.548
5-F	6.8		1.73			0.659	0.0218
unsubstituted	6.9		0.735			0.155	

[a] Experimental conditions: The second-order rate constants for the acetate and butylamine dependent reactions were determined in water or acetonitrile at 20 °C under pseudo-first order conditions as previously described. The reactions with 34E4 and BSA were performed in 40 mM phosphate, 100 mM NaCl, pH 7.4 and 20 °C.

Table 3. Relative Second Order Rate Constants and Brønsted Coefficients for the Decomposition of Substituted Benzisoxazoles

base/catalyst, medium	k_{rel}[a]	β_{lg}	r^2	no. of points
acetate, H_2O	1	-0.67 ± 0.01	0.998	8
acetate, CH_3CN	7.5×10^7	-0.95 ± 0.05	0.983	8
butylamine, H_2O	2.5×10^3	-0.53 ± 0.07	0.946	5
butylamine, CH_3CN	2.0×10^4	-0.86 ± 0.09	0.967	5
antibody 34E4, H_2O (pH 7.5)	4.1×10^8	-1.48 ± 0.13[b]	0.956	8
BSA, H_2O (pH 7.5)	1.8×10^6	-0.82 ± 0.07	0.946	10

[a] The second-order rate constant (k_{base} or k_{cat}/K_m) for the 5-NO_2 derivative. [b] Excluding 6-nitro, 5,6-dinitro, and 5,7-dinitrobenzisoxazoles, which deviate systematically from the correlation due to comparatively large K_m values (see Figure 2).

along with the pK_a values of the leaving group of the corresponding phenols and the rate constants measured in water and acetonitrile (MeCN) with different bases and catalysts. Table 3 lists the β_{lg} values derived from the plots shown in Figure 2. Excellent LFERs are found for the eliminations promoted by butylamine or acetate as base, in both water and acetonitrile solvents, and with the catalytic antibody 34E4 and bovine serum albumin (BSA) as catalysts.

The β_{lg} values for these correlations vary from -0.53 to -1.48. In each case, the reaction rate increases with decreasing salicylonitrile pK_a, indicating substantial transfer of negative charge to the ether oxygen of the benzisoxazole in the transition state. The reactions involving acetate and butylamine in water have the smallest β_{lg} values; they are least sensitive to the stability of the leaving group. The similarity of the values suggests that the structures and strengths of the base have little influence on the transition state structure and its solvation in water. The change to acetonitrile as solvent causes a 10^8 acceleration with acetate as base, but only a 10-fold effect with the amine base. Despite dramatically different effects on the rates with different bases, the Brønsted β_{lg} values are -0.9 to -1.0 for both acetate and butylamine in acetonitrile. The values are close to -1, so that the effect of leaving group stability is strongly felt in the transition state. However, the aqueous pK_a values are used for this correlation, while one would expect a larger spread of pK_a values for a related nonpolar solvent. In the lower dielectric environment, there is greater sensitivity to charge development at oxygen.

These results can be compared and contrasted with those obtained with the protein catalysts BSA and antibody 34E4. BSA accepts a wide variety of mono- and di-substituted benzisoxazoles as substrates (Table 2), and the Brønsted β_{lg}

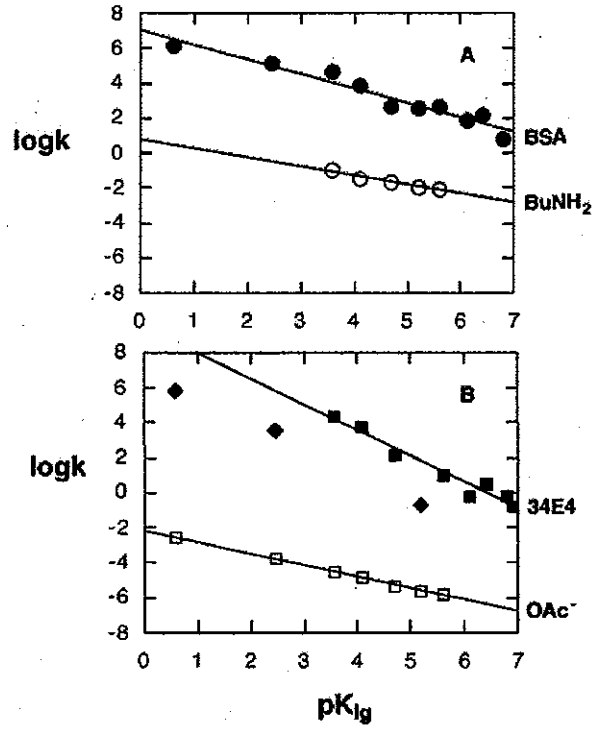

Figure 2. (A) Brønsted plot for the aqueous reaction of substituted benzisoxazoles with $BuNH_2$ (○) or with BSA (●). The apparent second-order rate constant $(k_{cat}/K_m)_{BSA}$ obtained at pH 7.4 was extrapolated to its maximum value using the known pH-dependence of the BSA-catalyzed reaction. (B) Brønsted plot for the aqueous reactions of BI with acetate (□) or 34E4 (■). The reactions of 34E4 with 5,7-dinitro-, 5,6-dinitro-, and 6-nitrobenzisoxazole (◆) deviate systematically from the correlation relating the other eight substrates.

value correlating these reaction rates is similar to that obtained with butylamine in acetonitrile. This suggests that the protein binding pocket that contains Lys222, the likely catalytic base,[9,17] presents a microenvironment to the developing phenoxide that is similar to that of acetonitrile.

Antibody 34E4 likewise accepts a wide range of substituted benzisoxazoles as substrates, but as shown in Figure 2, the reaction rate is unusually sensitive to leaving group effects. Eight of the eleven substrates tested are correlated with $\beta_{lg} = -1.5$, which is much larger than any of the other Brønsted coefficients. In this environment, the elimination rates respond more to substituent effects than aqueous pK values do. This mostly likely

(17) Carter, D. C.; Ho, J. X. *Adv. Prot. Chem.* **1994**, *45*, 153–203.

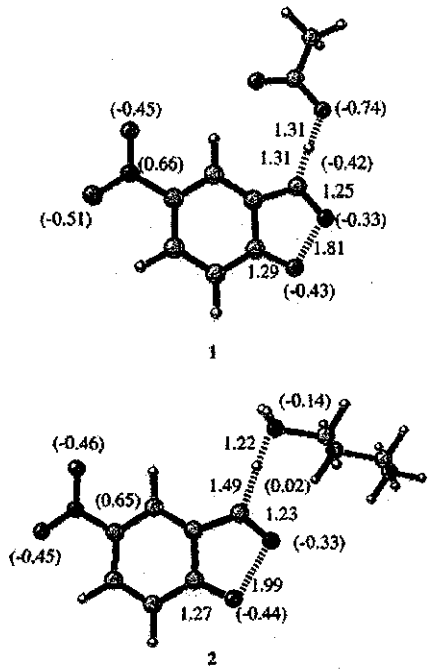

Figure 3. Computed transition states for reaction of acetate and butylamine with 4-nitrobenzisoxazole. Relevant bond lengths and charges are shown.

arises from the enhanced basicity of the phenoxide leaving group in a relatively nonpolar environment, which leads to a larger spread in phenoxide pK values than in water or acetonitrile and a β value greater than -1.

The Brønsted plot for k_{cat} similarly yields $\beta_{lg} = -1.5$ ($r^2 = 0.97$) as a consequence of the similar K_m values (100−200 μM) exhibited by these substrates. Benzisoxazoles containing a nitro substituent at the 6- or 7-position deviate negatively from the correlation in 34E4 shown in Figure 2 and appear to lie along a line that is roughly parallel to that through the data for the other substrates. These substrates have substantially larger K_m values than the others, suggesting that they adopt a different binding mode at the active site. However, the large kinetic isotope effect ($V/K^D = 5.7$) measured for the most reactive compound, 5,7-dinitrobenzisoxazole ($k_{cat} = 660\ s^{-1}$, $K_m = 1.0$ mM), shows that CH bond-breaking is still rate limiting for these substrates. The large β value for 34E4 indicates that the developing negative charge is relatively destabilized by the environment so that the substituent effects are very large, and reflect the very large role of substituent, rather than microenvironment, on charge stabilization. The results suggest that the local environment of 34E4 around the leaving group is effectively less polar than acetonitrile.

Quantum Mechanical Studies of the Base-Promoted Benzisoxazole Ring-Opening. Quantum mechanical calculations[18] and solvation energy estimations[19−22] were performed as described in the Experimental Section. The optimized geometries of the two transition states with acetate and butylamine as bases in the gas phase are shown in Figure 3. The proton is more completely transferred in the amine reaction, but the C−(H)−O and C−(H)−N distances are similar, at 2.62 and 2.71 Å, respectively. The lengths of the breaking N−O bonds in the five-membered ring are 1.81 and 1.99 Å in the two transition states, respectively. The charges on nitrogen (−0.33) and oxygen (−0.44) of the cleaving benzisoxazole ring are almost identical.

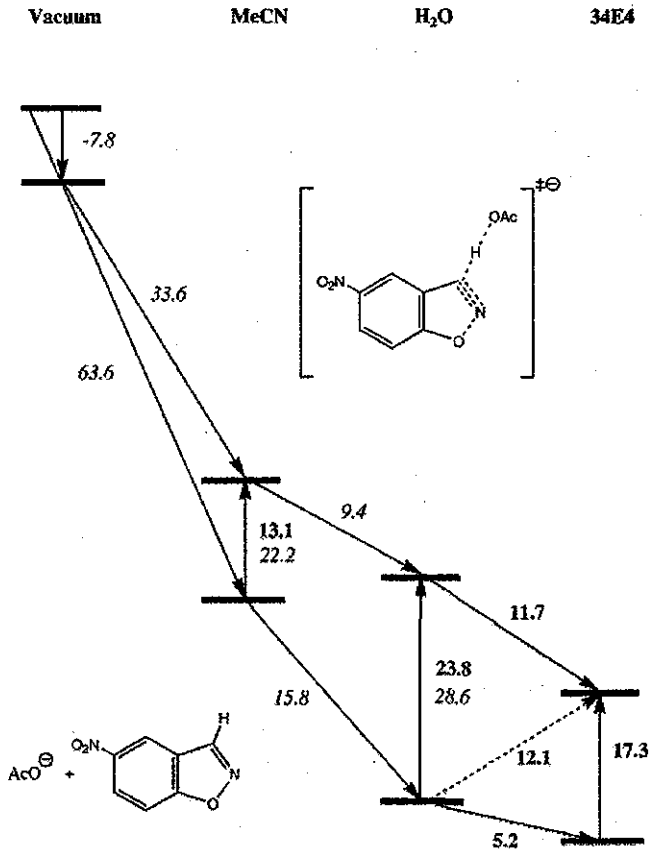

Figure 4. Free energy (ΔG) diagrams for reactions of acetate with 4-nitrobenzisoxazole in gas phase, acetonitrile, water, and antibody 34E4. Numbers in bold face are experimental values and those in italics are the averaged calculated values based on PCM and CPCM models.

Therefore, the E2 type geometry of the Kemp ring-opening does not change significantly with different bases.

The calculated activation barrier in the gas phase is −7.8 kcal/mol for the acetate catalyzed reaction, because there is an ion−molecule complex between the ionic reactant, acetate, and benzisoxazole, which is lower in energy than the reactants and the transition state for elimination. The conversion of this complex to the transition state has a normal positive activation barrier in solutions.

Solvation Energy Calculations. The calculated solvation free energies of acetate are all within 3 kcal/mol of the experimental aqueous solvation free energy of acetate (−77 kcal/mol).[23] The free energies of reactants and transition states in solvents are sums of the single point solvation free energies based on the

(18) Gaussian 98, Revision A.9, Frisch, M. J.; Trucks, G. W.; Schlegel, H. B.; Scuseria, G. E.; Robb, M. A.; Cheeseman, J. R.; Zakrzewski, V. G.; Montgomery, J. A.; Stratmann, Jr., R. E.; Burant, J. C.; Dapprich, S.; Millam, J. M.; Daniels, A. D.; Kudin, K. N.; Strain, M. C.; Farkas, O.; Tomasi, J.; Barone, V.; Cossi, M.; Cammi, R.; Mennucci, B.; Pomelli, C.; Adamo, C.; Clifford, S.; Ochterski, J.; Petersson, G. A.; Ayala, P. Y.; Cui, Q.; Morokuma, K.; Malick, D. K.; Rabuck, A. D.; Raghavachari, K.; Foresman, J. B.; Cioslowski, J.; Ortiz, J. V.; Baboul, A. G.; Stefanov, B. B.; Liu, G.; Liashenko, A.; Piskorz, P.; Komaromi, I.; Gomperts, R.; Martin, R. L.; Fox, D. J.; Keith, T.; Al-Laham, M. A.; Peng, C. Y.; Nanayakkara, A.; Challacombe, M.; Gill, P. M. W.; Johnson, B.; Chen, W.; Wong, M. W.; Andres, J. L.; Gonzalez, C.; Head-Gordon, M.; Replogle, E. S.; Pople, J. A. Gaussian, Inc., Pittsburgh, PA, 1998.
(19) Barone, V.; Cossi, M.; Tomasi, J. *J. Comput. Chem.* **1998**, *19*, 404−417.
(20) Miertus, S.; Scrocco, E.; Tomasi, J. *Chem. Phys.* **1981**, *55*, 117−129.
(21) JAGUAR (Schrödinger, Inc., Portland, OR) Version 4.0, 2000.
(22) "AMSOL 6.5", Hawkins, G. D.; Giesen, D. J.; Lynch, G. C.; Chambers, C. C.; Rossi, I.; Storer, J. W.; Rinaldi, D.; Liotard, D. A.; Cramer, C. J.; Truhlar, D. G.
(23) Pearson, R. G. *J. Am. Chem. Soc.* **1986**, *108*, 6109−6114.

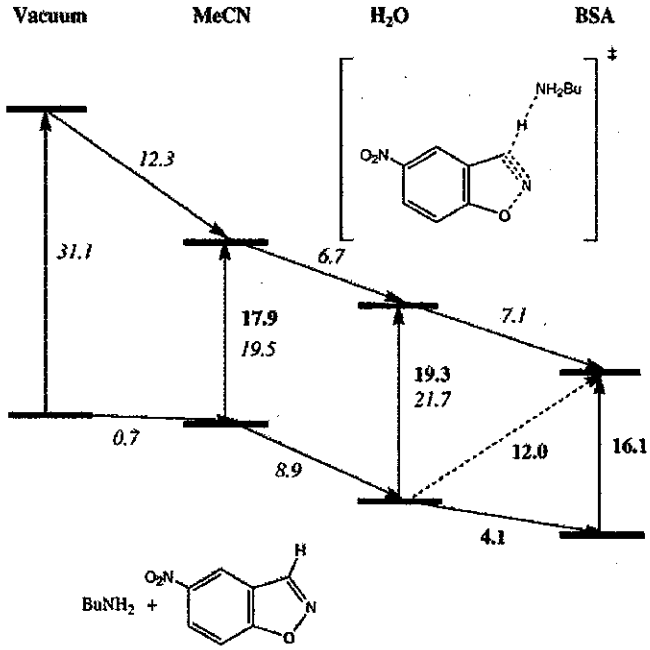

Figure 5. Free energy (ΔG) diagrams for reactions of butylamine with 4-nitrobenzisoxazole in the gas phase, acetonitrile, water and BSA. Numbers in bold face are experimental values and those in italics are the averaged calculated values based on PCM and CPCM models.

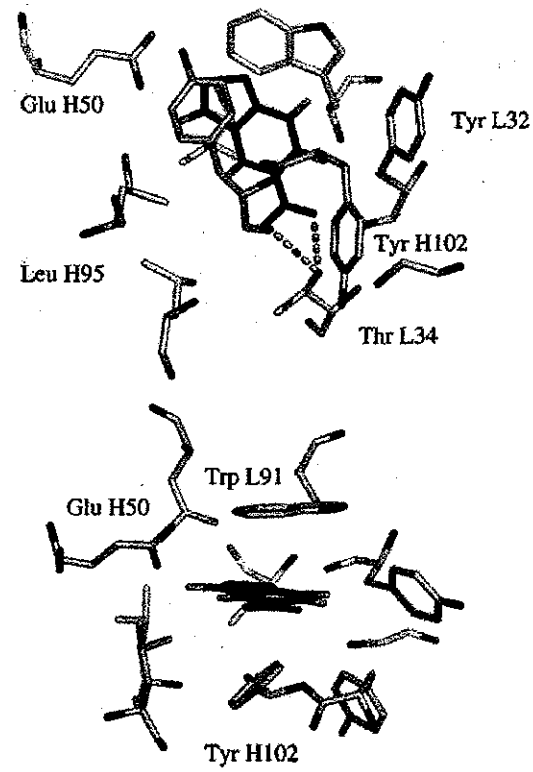

Figure 6. Docked binding mode of TS minus AcO^- in the 34E4 binding site. (a) Side view (b) Top view.

gas-phase geometries, and the relevant free energies in the gas phase. All of the methods overestimate the activation barriers in both water and MeCN. The CPCM model shows a change in the activation energy (7 kcal/mol) from water to acetonitrile which is closes to the experimental value (11 kcal/mol).

Figure 4 summarizes the energetics of acetate- and 34E4-promoted eliminations. CPCM calculations predict that acetate and benzisoxazole are stabilized by a total of 63.6 kcal/mol in acetonitrile, while the transition state **1** is solvated by only 33.6 kcal/mol. Because the reactants are stabilized much more than the transition state, the activation barrier changes from −7.8 kcal/mol in the gas phase to 22.2 kcal/mol in acetonitrile. The reactants and transition state are stabilized further by 15.8 and 9.4 kcal/mol, respectively, when changing the solvent from acetonitrile to water. The new activation barrier is calculated to be 28.6 kcal/mol, which is 6.4 kcal/mol higher than in acetonitrile, experiment shows an even larger activation barrier increase of 10.7 kcal/mol. Larger basis sets are likely to improve agreement with experiment. For the acetate-promoted process, the gas phase activation barrier (and consequently all the others) is decreased by 2 kcal/mol.

For the amine-catalyzed reaction, summarized in Figure 5, the activation barrier in the gas phase is 31.1 kcal/mol due to the difficulty of charge separation in the gas phase. The reactants are barely solvated by acetonitrile (0.7 kcal/mol), while the transition state is stabilized by 12.3 kcal/mol due to its high polarity. This leads to a smaller activation barrier (19.5 kcal/mol) in acetonitrile than in the gas phase. The additional changes of solvation free energies upon transfer from acetonitrile to water for reactants and transition state **2** are 8.9 and 6.7 kcal/mol, respectively. The resulting activation barrier in water (21.7 kcal/mol) is slightly higher than in acetonitrile, because the reactants are stabilized more than transition state. These calculations show good agreement with experiment for both acetonitrile and water.

Acetate has an experimental pK_a value of 4.8 in water and 22.3 in acetonitrile,[24] and this large change is reflected in the large rate acceleration of the elimination in acetonitrile. However, experiment and calculation show that there is only a 2∼3 kcal/mol barrier change for the amine-catalyzed reaction. The small activation barrier change in the amine-catalyzed reaction is related to the smaller pK fluctuation from 10.8 in water to 18.3 in acetonitrile.[23]

Transfer of Substrates and Transition States from Water to Protein. The binding energies for reactants, estimated from measured K_m values, are 5.2 and 4.1 kcal/mol for 34E4 and BSA, respectively. The calculated free energy corresponding to k_{cat}/K_m is 12.1 kcal/mol for the reaction catalyzed by 34E4 and 12.0 kcal/mol for BSA. These results are also shown in Figures 4 and 5. According to the thermodynamic cycle, 34E4 and BSA stabilize the transition states by 11.7 and 7.1 kcal/mol relative to water, respectively. In acetate- and amine-catalyzed reactions, both the reactants and transition states are stabilized upon proceeding along the series from vacuum to acetonitrile, water, and protein. The protein catalysis occurs by lowering the free energy of the transition state in the protein complex more than the substrate in the protein complex. A similar trend was also found in our study of another solvent sensitive reaction, the antibody-catalyzed Kemp decarboxylation.[25]

Docking Studies with 34E4. To explore in detail the mechanism of antibody catalysis, the substrate and transition state were docked into the binding sites of 34E4. In the absence of a crystal structure for 34E4, we used a homology-based model

(24) Kolthoff, I. M.; Chantoon, M. K.; Bhowmik, S. *J. Am. Chem. Soc.* **1968**, *90*, 23−28.
(25) Ujaque, G.; Tantillo, D.; Hu, Y.; Houk, K.; Hotta, K.; Hilvert, D. *J. Comput. Chem.* **2003**, *24*, 98−110.

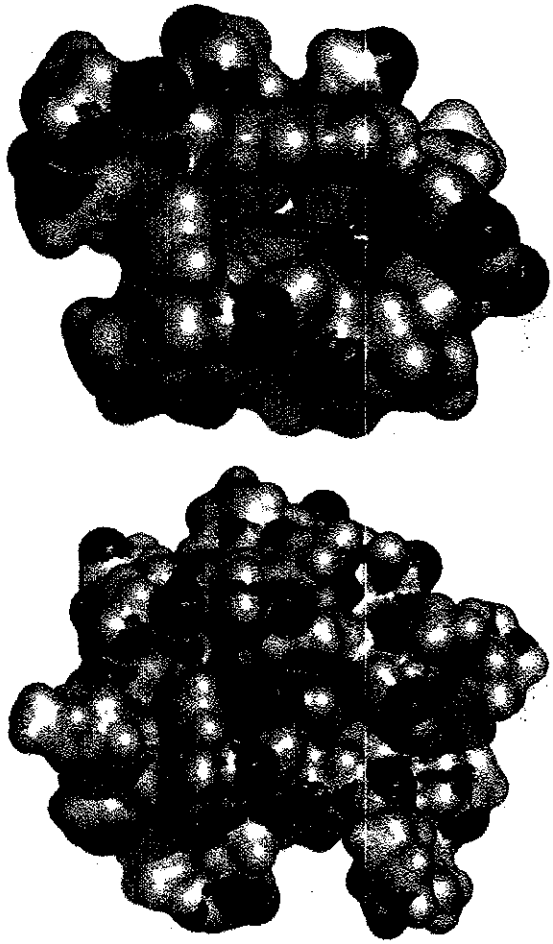

Figure 7. 34E4 surface including residues within 5 Å (top) and 8 Å (bottom) of the docked transition state.

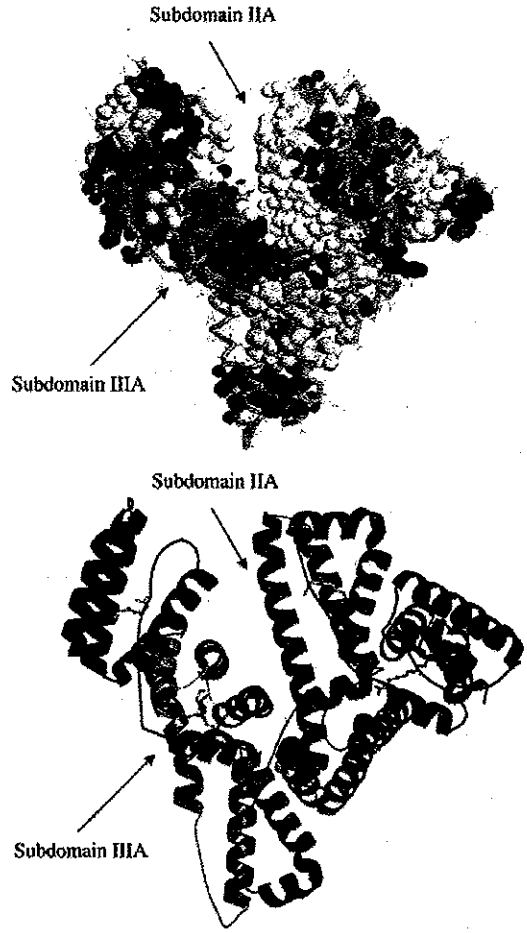

Figure 8. Human serum albumin. (a) Binding pockets and cavities calculated by CAST (b) The docked transition state and the myristic acid inhibitor.

based on the sequence of 34E4 obtained here (see Experimental Section). Figure 6 shows the best transition state docking mode for the acetate-catalyzed reaction in 34E4 in both side and top views. It has an estimated free energy of binding of −7 kcal/mol, according to the AUTODOCK free energy scoring function. In the vicinity of the benzisoxazole moiety, there are mostly hydrophobic residues. The nitro group is buried in the bottom of the 34E4 binding pocket, and forms two hydrogen bonds with Thr L34. The tight steric fit of the substrate within the pocket also suggests why substituents at the 6-position influence substrate binding (K_m) to a considerable extent in kinetic experiments (Table 2). Near the entrance to the binding site, the benzisoxazole transition moiety is surrounded by Tyr L32, Trp L91, Tyr H102, Tyr H103, and Glu H50, all of which are within 5 Å of the transition state. A potential base, Glu H50 is placed perfectly to deprotonate the benzisoxazole and initiate ring-opening. The distance of the nearest carboxylate oxygen from the transferring proton is 2.5 Å. The proposed role in catalysis is consistent with preliminary mutagenesis results showing that activity is abolished when GluH50 is substituted with glutamine.[27]

Figure 7 shows the solvent accessible surfaces of the 34E4 binding pocket including residues within 5 Å (top) or 8 Å (bottom) of the transition state. The transition state is trapped deeply inside the complementary binding pocket, which has a very narrow entrance formed by several hydrophobic residues. The second view shows that the transition state in 3D representation is in relatively tight contact with the surroundings. The region of negative electrostatic potential (red) is concentrated on the Glu H50 side, near where the proton of the benzisoxazole is located.

Antibody 34E4 provides a preorganized microenvironment made of hydrophobic and polar residues around the reaction center, with the basic site oriented for deprotonation of the benzisoxazole. The oxygen of the benzisoxazole ring is situated so as to be solvated by external water as it is transformed into cyanophenoxide.

Serum Albumin Catalysis. Serum albumins are ubiquitous proteins in the blood stream; albumins bind various small molecules in multiple binding sites. Hilvert and Kirby's experiment show that BSA and human serum albumin (HSA) have similar effects on the benzisoxazole elimination, and there is a binding site with lysine group present in each case.[5] Because the BSA crystal structure is unavailable, we used the HSA crystal structure for the docking study.

Two binding pockets with the highest CAST score (see Experimental Section) are the most likely binding sites (Figure 8). Subdomains IIA and IIIA, shown as light yellow and light blue, are also the two sites that have been proposed to bind small heterocyclic substrates such as warfarin experimen-

(26) Morris, G. M.; Goodsell, D. S.; Halliday, R. S.; Huey, R.; Hart, W. E.; Belew, R. K.; Olson, A. J. *J. Comput. Chem.* **1998**, *19*, 1639−1662.
(27) Seebeck, F., unpublished results.

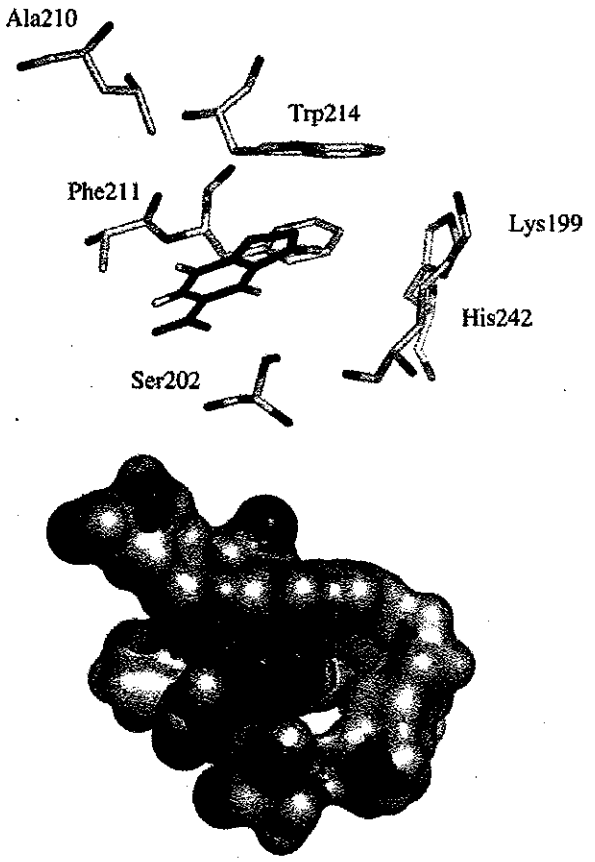

Figure 9. Transition state moiety in HSA subdomain IIA. (a) Residues within 5 Å of the transition state (b) Surface representation of residues within 5 Å of the transition state.

tally.[29,30] The five myristic acids determined from the same crystal structure are shown in the second view (Figure 8b). Although there are lysine residues on the HSA surface, none of them can be considered as effective catalytic bases because of their high pK_a values on the protein surface. There is one lysine in subdomain IIA and no lysine residues inside the subdomain IIIA. Consequently, we focused our attention on the IIA subdomain.

Autodock produced a binding mode that is shown in Figures 9 and 10. The average estimated free energy of binding is −6 kcal/mol. Figure 9 shows stick and space-filling renderings of the protein with the transition state surrounded by residues in the cleft of subdomain IIA within 5 Å. The pocket has mainly nonpolar residues including Trp 214, Ala 219, Phe 211, Ser 202, His 242, and the putative base, Lys 199. The latter is 5.4 Å away from the transferring hydrogen. The only tryptophan in albumin, Trp214, has $\pi-\pi$ interactions with benzisoxazole aromatic ring. There is barely enough room for the transition state to stay in such a steep and narrow pocket. This can be seen from the comparison of 5 Å (Figure 9b) and 8 Å (Figure 10) surfaces. The transition state resides in the concave part of the binding pocket. Such a binding mode is not easily accessible from outside without conformational changes of the albumin upon binding the ligand. Lys 195 is located in subdomain IIA

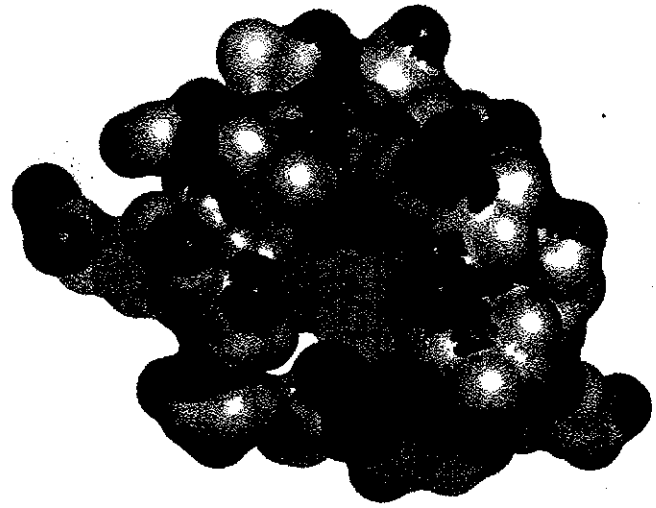

Figure 10. Surface representation of residues within 8 Å of the transition state.

next to Lys 199. The protonation states of these two lysine groups have been studied both experimentally and theoretically. The combination of a neutral Lys 199 and protonated Lys 195 is the most favored one since they can form a hydrogen bond with water.[31] Experiments show that Lys 199 has a low pK_a (~8).[32] Therefore, we postulate that Lys 199 is the catalytic group in human serum albumin, whereas Lys222 is the catalytic group in bovine serum albumin. Experiments also indicate that HSA loses most of its catalytic ability upon Lys199 modification,[5] confirming the predictions from docking experiments.

Conclusion

The mechanisms of catalysis of the Kemp elimination have been elucidated for reactions occurring in two proteins, and the rates have been computed in aqueous and nonpolar solvents. Antibody 34E4 catalyzes this reaction by the alignment of catalytic base Glu H50 and substrate benzisoxazole within a relatively nonpolar pocket. Similarly, HSA has a deep nonpolar pocket at subdomain IIA with Lys 199 that can deprotonate 5-nitrobenzisoxazole.

An analogy between enzymes and organic solvents is often made, but the heterogeneous microenvironment of a protein pocket is clearly different from free solvent molecules in that its fixed structure can be tuned to interact with and stabilize disparate components of a reacting molecule. The efficiency of these biological catalysts derives from having a catalytic base geometrically positioned in a generally nonpolar active site, a consequence of successful hapten design in 34E4, but serendipitous in albumin. From the evolutionary perspective, there is no fundamental difference between our specific residue positioning argument and Kirby's more recent proposal of a specific medium effect.[9,33] The specific medium effect involves dispersion and electrostatic interactions with the transition state, which is a necessary outcome of the specific group positioning. The ultimate biological catalyst must utilize a perfect match

(28) (a) Liang, J.; Edelsbrunner, H.; Woodward, C. *Protein Science* **1998**, *7*, 1884−1897. (b) Liang, J.; Edelsbrunner, H.; Fu, P.; Sudhakar, P. V.; Subramaniam, S. *Proteins* **1998**, *33*, 1−17.
(29) Bhattacharya, A. A.; Grune, T.; Curry, S. *J. Mol. Biol.* **2000**, *303*, 721−732.
(30) Zaton, A. M. L.; Villamor, J. P. *Chem.-Biol. Interact* **2000**, *124*, 1−11.
(31) (a) Diaz, N.; Suarez, D.; Sordo, T. L.; Merz, Jr., K. M. *J. Med. Chem.* **2001**, *44*, 250−260. (b) Bhattacharya, A. A.; Petitpas, I.; Twine, S.; East, M.; Curry, S. *J. Biol. Chem.* **2001**, *276*, 22 804−809.
(32) (a) Gerig, J. T.; Reiheimer, J. D. *J. Am. Chem. Soc.* **1975**, *97*, 168−173. (b) Gerig, J. T.; Katz, K. E.; Reinheimer, J. D. *Biochim. Biophys. Acta* **1978**, *534*, 196−209.
(33) Hollfelder, F.; Kirby, A. J.; Tawfik, D. S. *J. Am. Chem. Soc.* **1997**, *119*, 9578−9579.

between the catalytic group and the transition state plus an elaborate active site made of polar and nonpolar groups, which provides favorable interactions with the transition state including electrostatics, solvation and other factors.[34] The most important feature for catalysis is the assembly of catalytic functionality, here the basic site, with appropriate orientation and reactivity. Of course catalysts that accidentally have an appropriate environment do exist, such as albumins in this case.

Catalytic antibodies represent a successful effort to biological catalyst design for nonbiological reactions. The problems in such design and execution are known[5] to be difficult but not insoluble.[36,37] A remaining challenge is how to use the programmable nature of the antibody pocket along with medium effects to act in concert with other active site parameters. Careful design by increasing the strength of the catalytic base through desolvation and by providing specific stabilizing interactions with the leaving group such as forming hydrogen bonds with phenoxide, should lead to better catalysts for such a solvent sensitive reaction.[38]

Experimental Section

Synthesis of Substituted Benzisoxazoles. Unsubstituted benzisoxazole and the 5-nitro-, 6-nitro-, 5,7-dinitro-, 5-chloro-, and 6-chloro-substituted derivatives were prepared according to the literature.[1a,39] 4-Cyano- and 4-fluorosalicylaldehyde were prepared from the corresponding phenols by a Duff reaction;[40] 4,5-dichlorosalicylaldehyde was prepared by a Reimer–Tiemann reaction.[41] The substituted salicylaldehydes were converted to benzisoxazoles by a standard literature procedure.[39b]

5-Cyanobenzisoxazole. ^{1}H NMR (300 MHz, $CDCl_3$) δ 7.76 (q, 1H), 7.84 (q, 1H), 8.16 (d, 1H), 8.83 (d, 1 H). MS FABM$^+$ 145 (M^++H^+). mp 245 °C (decomp.).

5,6-Dichlorobenzisoxazole. ^{1}H NMR (300 MHz, $CDCl_3$) δ 7.80 (d, 1H), 7.85 (s, 1H), 8.68 (d, 1H). MS FABM$^+$ 187/189 (M^++H^+), 210/212 (M^++Na^+). mp 92 °C (sub.).

5-Fluorobenzisoxazole. ^{1}H NMR (300 MHz, $CDCl_3$) δ 7.32 (q, 1H), 7.38 (q, 1H), 7.59 (q, 1H), 8.7 (d, 1 H). MS FABM$^+$ 139 (M^++H^+). mp 68 °C (sub.).

5,6-Dinitrobenzisoxazole. 6-Nitrobenzisoxazole (200 mg) was dissolved in ice-cooled cH_2SO_4 (1.6 mL). Fuming nitric acid (200 μl) was added dropwise, and the reaction mixture was heated at 80 °C for 30 min. The starting material was completely consumed. The reaction mixture was poured onto ice and then extracted immediately with methylene chloride. The organic layer was dried and purified by silica gel chromatography using methylenechloride as eluent to give 142 mg of the desired product in 56% yield. ^{1}H NMR (300 MHz, $CDCl_3$) δ 8.17 (q, 1H), 8.52 (d, 1H), 9.15 (d, 1H). MS FABM$^+$ 210 (M^++H^+). mp 112 °C.

5-Nitro-6-chlorobenzisoxazole. 6-Chlorobenzisoxazole was nitrated at the 5-position by the same method used to prepare 5,6-dinitrobenzisoxazole in 62% yield. ^{1}H NMR (300 MHz, $CDCl_3$) δ 7.88 (d, 1H), 8.36 (d, 1H), 8.86 (d, 1H). MS FABM$^+$ 198/200 (M^++H^+). mp 106 °C.

Kinetic Analyses. All kinetic experiments were performed at 20 °C. Fast reactions were measured by stopped flow techniques. The reactions were initiated by adding the benzisoxazole substrate to the reaction mixture and product formation was monitored spectrophotometrically at the following wavelengths: 5,7-dinitro (352 nm), 5,6-dinitro (380 nm), 5-nitro-6-chloro (380 nm), 5-nitro (380 nm), 5-cyano (324 nm), 6-nitro (404 nm), 5,6-dichloro (342 nm), 6-chloro (329 nm), 5-chloro (339 nm), 5-fluoro (338 nm), and unsubstituted (325 nm). Extinction coefficients were measured for each compound under the reaction conditions. The second-order rate constants for the acetate and butylamine-dependent reactions were determined in water or MeCN at 20 °C. Pseudo-first-order rate constants were plotted against acetate or butylamine concentration, and the slope of these plots gave the second-order rate constant for the base-catalyzed reaction. The reactions with 34E4 and BSA were performed in 40 mM phosphate, 100 mM NaCl, pH 7.4 and 20 °C. Initial velocities were calculated by standard linear-regression analysis using the initial linear portion of absorbance vs time plots and were corrected for background activity. The k_{cat} and K_m values were calculated by fitting the kinetic data to the Michaelis–Menten equation using the program KaleidaGraph. Two percent acetonitrile was used to dissolve the substrate for all reactions in aqueous medium. Crystallized BSA, treated to remove bound lipids, was purchased from Sigma and used without further purification; 34E4 was isolated and purified as previously described.

Cloning of the Antibody Genes. Poly (A)$^+$ mRNA was isolated from the hybridoma producing antibody 34E4.[2] A cDNA library was constructed with the Great Lengths cDNA synthesis kit (Clontech). The V_L and V_H genes were cloned using the polymerase chain reaction with the following primers: V_L sense, GTACATTT*GCTCTTC*GGTTCACAGGCTGTTGTGACTCAGGAA (the *Sac* I restriction site is in italics); V_L anti-sense, ATGAGTTTTTGTTCT*GCGGCCGC*CTTGGGCTGACCTAGGACAGT (*Not* I); V_H sense AGGTCCAGCT-G*CTCGAG*TCTGG (*Xho* I); V_H anti-sense GTTCTG*ACTAGT*-GGGCACTCTGGGCTC (*Spe* I). The amplified fragments were purified, cloned into appropriate sites in the vector p4xH-M13[42] and sequenced. The resulting expression plasmid, p4xH-34E4, allows production of 34E4 as a chimeric murine-human Fab fragment in which the V_L and V_H segments of the catalytic antibody are fused to human Cκ and gamma C_H1 regions, respectively.[42]

The antibody sequences for the variable segments of 34E4 are given in Chart 1.

Construction of a Homology Model. A search of the structure database identified antibodies HC19 (1gig.pdb)[43] and J539 (2fbj.pdb)[44] as having the highest sequence similarity to the 34E4 V_L and V_H domains, respectively. Because HC19 and 34E4 have CDR H3 loops that are the same length and that possess reasonable sequence similarity (28.6%), modeling of the V_L–V_H interface[45] is facilitated. A least-squares fit of the V_H domains of HC19 and J539, minus the CDR H3 loop, allowed overlay of the two molecules with a rmsd. of 1.40 Å for all Cα atoms except those of the CDR L1 (residues L24 to L34) and H3 (residues H95 to H102). In this overlay, the V_H domains of the two antibodies were superimposed with rmsd. of 0.88 Å for all non-CDR H3 Cα atoms, whereas the V_L domains were overlaid with rmsd. of 1.37 Å for all non-CDR L1 Cα atoms. In particular, the residues near the V_L/V_H interface from the two molecules, namely residues L42-L46, L94-L100, H43-H50, H58-H61, and H103-H105 (27 residues in total), coincided with each other with rmsd. of 0.87 Å for all Cα atoms. Accordingly, visual inspection of the interface between the HC19 V_L and J539 V_H domains revealed that no significant steric interference was introduced by the way the two domains were put together. After

(34) Houk, K. N.; Leach. A. G.; Kim, S. P.; Zhang, X. *Angew Chem., Int. Ed.* **2003**, *42*, 4872–4897.
(35) Zhang, X.; Houk, K. N., submitted for publication.
(36) Tantillo, D. J.; Houk, K. N. *J. Org. Chem.* **1999**, *64*, 3066–3076.
(37) Barbany, M.; Gutierrez-de-Teran, H.; Sanz, F.; Villa-Freixa, J.; Warshel, A. *ChemBioChem* **2003**, *4*, 277–285.
(38) Parker, A. J. *Chem. Rev.* **1969**, *69*, 1–32.
(39) (a) Kemp, D. S.; Woodward R. B. *Tetrahedron* **1965**, *21*, 3019–3035. (b) Casey, M. L.; Kemp, D. S.; Paul, K. G.; Cox, D. D. *J. Org. Chem.* **1973**, *38*, 2294–2301.
(40) Suzuki, Y.; Takahashi, H. *Chem. Pharm. Bull.* **1983**, *31*, 1751–1753.
(41) Postmus, C.; Kaye, I. A.; Craig, C. A.; Matthews, R. S. *J. Org. Chem.* **1964**, *29*, 2693–2698.
(42) Ulrich, H. D., Patten, P. A., Yang, P. L., Romesberg, F. E., & Schultz, P. G. *Proc. Natl. Acad. Sci. U.S.A.* **1995**, *92*, 11 907–11 911.
(43) Bizebard, T.; Daniels, R.; Kahn, R.; Golinellipimpaneau, B.; Skehel, J. J.; Knossow, M. *Acta Crystallog.* **1994**, *D50*, 768–777.
(44) Suh, S. W.; Bhat, T. N.; Navia, M. A.; Cohen, G. H.; Rao, D. N.; Rudikoff, S.; Davies, D. R. *Proteins: Struct. Funct. Genet.* **1986**, *1*, 74–80.
(45) Stanfield, R. L.; Takimoto-Kamimura, M., Rini, J. M.; Profy, A. T.; Wilson, I. A. *Structure* **1993**, *1*, 83–93.

Chart 1

34E4 light chain variable domain

1	2	3	4	5	6	7	8	9	10	11	12
gln	ala	val	val	thr	gln	glu	ser	ala	- - -	leu	thr
13	14	15	16	17	18	19	20	21	22	23	**24**
thr	ser	pro	gly	glu	thr	val	thr	leu	thr	cys	arg
25	**26**	**27**	**27A**	**27B**	**27C**	**28**	**29**	**30**	**31**	**32**	**33**
ser	ser	ser	gly	ala	val	thr	thr	ser	asn	tyr	ala
34	35	36	37	38	39	40	41	42	43	44	45
thr	trp	val	gln	glu	lys	pro	asp	his	leu	phe	thr
46	47	48	49	**50**	**51**	**52**	**53**	**54**	**55**	**56**	57
gly	leu	ile	gly	gly	thr	asn	lys	arg	ala	pro	gly
58	59	60	61	62	63	64	65	66	67	68	69
val	pro	ala	arg	phe	ser	gly	ser	leu	ile	gly	asp
70	71	72	73	74	75	76	77	78	79	80	81
arg	ala	ala	leu	thr	ile	thr	gly	ala	gln	thr	glu
82	83	84	85	86	87	88	**89**	**90**	**91**	**92**	**93**
asp	glu	ala	ile	tyr	phe	cys	ala	leu	trp	asn	ser
94	**95**	**96**	**97**	98	99	100	101	102	103	104	105
asn	his	leu	val	phe	gly	gly	gly	thr	lys	leu	thr
106	106A	107	108	109	110						
val	leu	gly	gln	pro	(lys)*						

34E4 heavy chain variable domain

1	2	3	4	5	6	7	8	9	10	11	12
(glu)	val*	(lys)*	leu	leu	glu	ser	gly	gly	gly	leu	ala
13	14	15	16	17	18	19	20	21	22	23	24
gln	pro	gly	gly	ser	leu	lys	leu	ser	cys	ala	ala
25	26	27	28	29	30	**31**	**32**	**33**	**34**	**35**	36
ser	gly	phe	asp	phe	arg	arg	tyr	trp	met	thr	trp
37	38	39	40	41	42	43	44	45	46	47	48
val	arg	gln	ala	pro	gly	lys	gly	leu	glu	trp	ile
49	**50**	**51**	**52**	**52A**	**53**	**54**	**55**	**56**	**57**	**58**	**59**
gly	glu	ile	asn	pro	asp	ser	arg	thr	ile	asn	tyr
60	**61**	**62**	**63**	**64**	**65**	66	67	68	69	70	71
met	pro	ser	leu	lys	asp	lys	phe	ile	ile	ser	arg
72	73	74	75	76	77	78	79	80	81	82	82A
asp	asn	ala	lys	asn	ser	leu	tyr	leu	gln	leu	ser
82B	82C	83	84	85	86	87	88	89	90	91	92
arg	leu	arg	ser	glu	asp	ser	ala	leu	tyr	tyr	cys
93	94	**95**	**96**	**97**	**98**	**99**	**100**	**100A**	**B**	**C**	**D**
val	arg	leu	asp	phe	asp	val	tyr	asn	his	tyr	tyr
E	**F**	**101**	**102**	103	104	105	106	107	108	109	110
val	leu	asp	tyr	trp	gly	gln	gly	thr	ser	val	thr
111	112	113									
val	ser	ser									

the superimposition of the HC19 V_L and J539 V_H domains, residues H90 to H104 (the CDR H3-containing loop) of the J539 V_H domain were replaced by the corresponding loop residues from HC19 to form a HC19 V_L-J539 V_H chimera with the H3 loop from HC19. All residues were then manually modified, or mutated, to reflect the 34E4 sequence. For the "mutated" residues, the side-chain rotamer that gave the best fit to the local environment as judged by visual inspection was chosen. Other known structures were also consulted in remodeling the local sequence environment around the mutated residues when the change required a significant structural alteration. For example, replacing Met^{H82} with a branched leucine in the J539 V_H domain caused a steric clash with the surrounding residues. However, structural information from antibody CHA255 (1ind.pdb),[46] which has a leucine residue at position H82, helped resolve the problem.

Quantum Mechanical Methods. Both transition state geometries were optimized in the gas phase with Density Functional Theory (DFT)[47] at B3LYP/6-31+G(d) level with GAUSSIAN 98.[18] CHELPG[48] charges were obtained at B3LYP/6-31+G(d) level. Several solvation models including CPCM,[19] a polarizable conductor-like solvation model, PCM,[20] a polarizable continuum model, a Poisson–Boltzmann (PB) model[21] and the Cramer–Truhlar SM5.2R solvation model[22] were compared for solvation calculations on acetate-catalyzed reaction (Table 4). All solvation energies from continuum models (PCM and CPCM) are single point energies computed based on the geometries in the gas phase.

Table 4. Comparison of Experimental and Calculated Solvation Free Energies and Nitrobenzisoxazole Elimination Activation Energies for Acetate-Catalysis with Different Theoretical Models

	solvation free energy in H_2O (kcal/mol)				solvation free energy in CH_3CN (kcal/mol)			
	AcO^-	NBI	TS	$\Delta\Delta G^{\ddagger}$	AcO^-	NBI	TS	$\Delta\Delta G^{\ddagger}$
CPCM[a]	−74.1	−5.2	−43.0	28.6	−63.0	−0.6	−33.6	22.2
PCM[a]	−75.3	−6.7	−43.5	30.7	−63.4	−0.6	−33.6	22.6
PB[b]	−77.4	−5.7	−46.4	28.9	−75.1	−12.4	−54.4	25.3
SM5.2R[c]	−77.3	−11.4	−51.6	29.3	−75.6	−15.7	−56.3	27.2
experiment	−77.0[d]			23.8	−62.7[e]			13.1

[a] B3LYP/6-31+G* with CPCM or PCM solvation models in Gaussian 98. [b] B3LYP/6-31+G* with Poisson–Boltzmann solvation model in Jaguar 4.0.[21] [c] AM1 with SM5.2R solvation model in AMSOL 6.5.[22] [d] Ref 23. [e] Pliego, Jr., J. R.; Riveros, J. M. *Phys. Chem. Chem. Phys.* **2002**, *4*, 1622.

Docking Calculations. Autodock 3.0[26] was employed for docking purposes. Autodock uses a hybrid Lamarckian genetic algorithm (LGA) for docking and predicts the best binding modes according to an empirical scoring function that predicts the binding energy. Acetate was left out purposely from the gas-phase transition state docking experiments, since a carboxylate of an aspartate or glutamate in the binding site is considered to be the base. CHELPG charges were taken from the computed transition state structure in the gas phase. The receptor is fixed in all the dockings and represented by grid maps. The transition states do not have any torsional degrees of freedoms because of their structural rigidity. A total of 100 ga-run were conducted in each case and resulting conformations were clustered with 1 Å root-mean-square deviations (RMSD). The representative docked conformation of the best cluster in terms of binding free energy and population was chosen as the final binding mode.

Location of Binding Sites in HSA. The CASTp program was used to locate possible binding cavities and pockets for albumin using a solvent probe (sphere of 1.4 Å) analytically.[28] Multiple binding pockets and cavities for HSA (PDB ID: 1BJ5) have been found as shown in Figure 8 (top). This crystal structure includes five bound myristic acids. These were removed for the CASTp analysis. The spheres represent the surfaces of the key C, N, and O atoms that define the boundary between bulk solvent and protein pockets or cavities.

Acknowledgment. We thank Jim Na (Pfizer, La Jolla), Jeehiun K. Lee (Rutgers), and Qiaolin Deng (Merck) for preliminary results and extensive discussions. We are grateful to the National Institute of General Medical Sciences, National Institutes of Health (D.H. and K.N.H.) and National Science Foundation (K.N.H.) for financial support of this research and to the Naito Foundation (Tokyo, Japan) for a postdoctoral fellowship to K.K. We owe special thanks to UCLA Academic Technology Services (Y.H. and K.N.H.) and ETH and Novartis (D.H.).

JA0490727

(46) Love, R. A.; Villafranca, J. E.; Aust, R. M.; Nakamura, K. K.; Jue, R. A.; Major, Jr., J. G.; Radhakrishnan, R.; Butler, W. F. *Biochemistry* **1993**, *32*, 10 950–10 959.

(47) (a) Becke, A. D. *J. Chem. Phys.* **1993**, *98*, 5648–5652. (b) Lee, C. T.; Yang, W. T.; Parr, R. G. *Phys. Rev. B* **1988**, *37*, 785–789.

(48) (a) Chirlian, L. E.; Francl, M. M. *J. Comput. Chem.* **1987**, *8*, 894–905. (b) Breneman, C. M.; Wiberg, K. B. *J. Comput. Chem.* **1990**, *11*, 361–373.

THE JOURNAL OF BIOLOGICAL CHEMISTRY
Vol. 279, No. 20, Issue of May 14, pp. 21533–21542, 2004
Printed in U.S.A.

Regulation of Immature Protein Dynamics in the Endoplasmic Reticulum*

Received for publication, February 9, 2004, and in revised form, February 19, 2004
Published, JBC Papers in Press, February 19, 2004, DOI 10.1074/jbc.M401403200

Asako Kamada‡§, Hisao Nagaya§¶, Taku Tamura§¶, Masataka Kinjo‖, Hai-Ying Jin‡, Toshiharu Yamashita‡, Kowichi Jimbow‡, Hideo Kanoh, and Ikuo Wada§¶‡‡**

*From the Departments of ‡Dermatology and **Biochemistry, Sapporo Medical University School of Medicine, Sapporo 060-8556, Japan, the §Core Research for Evolutional Science and Technology, JST, Japan, the ¶Department of Cell Science, Institute of Biomedical Sciences, Fukushima Medical University School of Medicine, Fukushima 960-1295 Japan, and the ‖Research Institute for Electronic Science, Hokkaido University, Sapporo 060-0812, Japan*

The quality of nascent protein folding *in vivo* is influenced by the microdynamics of the proteins. Excessive collisions between proteins may lead to terminal misfolding, and the frequency of protein interactions with molecular chaperones determines their folding rates. However, it is unclear how immature protein dynamics are regulated. In this study, we analyzed the diffusion of immature tyrosinase in the endoplasmic reticulum (ER) of non-pigmented cells by taking advantage of the thermal sensitivity of the tyrosinase. The diffusion of tyrosinase tagged with yellow fluorescence protein (YFP) in living cells was directly measured using fluorescent correlation spectroscopy. The diffusion of folded tyrosinase in the ER of cells treated with brefeldin A, as measured by fluorescent correlation spectroscopy, was critically affected by the expression level of tyrosinase-YFP. Under defined conditions in which random diffusional motion of folded protein was allowed, we found that the millisecond-order diffusion rate observed for folded tyrosinase almost disappeared for the misfolded molecules synthesized at a nonpermissive high temperature. This was not because of enhanced aggregation at the high temperature, as terminally misfolded tyrosinase synthesized in the absence of calnexin interactions showed comparable, albeit slightly slower, diffusion. Yet, the thermally misfolded tyrosinase was not immobilized when measured by fluorescence recovery after photobleaching. In contrast, terminally misfolded tyrosinase synthesized in cells in which α-glucosidases were inhibited showed extensive immobilization. Hence, we suggest that the ER represses random fluctuations of immature tyrosinase molecules while preventing their immobilization.

The maturation of proteins in the secretory pathway requires various sequential reactions including suppression of backward movements through the translocational channel by BiP (1); cleavage of the signal sequence and attachment of *N*-linked oligosaccharides (2); the prevention of nonproductive folding intermediates by various molecular chaperones (3); disulfide shuffling by disulfide isomerases possessing chaperone activity (4, 5); and proline isomerization (6). When these processes are not completed, proteins are disposed eventually. Recent extensive studies have been revealing the underlying molecular mechanisms of this destruction (7–11). However, there are also misfolded proteins that are able to maintain reversible folding for several hours after synthesis but somehow fail to exit the ER.[1] A temperature-sensitive ts045 variant of the vesicular stomatitis virus glycoprotein (VSVG) is the best known example (12–14). It was thought that the defect in the exit of this glycoprotein from the ER and its transport to the Golgi could be explained by (*a*) uncompleted interactions of cargo proteins with the "ER matrix," which is composed of various chaperones and folding enzymes (15, 16) or (*b*) misfolded aggregates (13) that are too large to enter the COPII-coated ER exit sites. However, measurements of the misfolded VSVG mutant in living cells using fluorescence recovery after photobleaching (FRAP) (17) surprisingly showed that the thermal-induced misfolding caused no significant loss of lateral mobility (18). While various models can be conceived to explain the results, the study at least eliminated the possibility that the misfolded VSVG failed to exit because it is tethered to the immobile ER matrix (19).

Movements of newly synthesized proteins could affect their folding *per se*. Collision of two molecules exposing hydrophobic patches on their surfaces could result in the formation of aggregates. Also, folding rates depend on the frequency of collision with molecular chaperones. Hence, it is expected that the mobility of proteins during folding is regulated in living cells. However, this is hard to measure by FRAP because FRAP records the average motion of a mass population and its time resolution is not sufficient for complicated dynamics including submillisecond diffusion. For measuring such random diffusional motion of an individual protein, fluorescence correlation spectroscopy (FCS) is, at present, the only practical method (20–22). FCS detects fluctuation of the fluorescence intensity in a confocally defined volume with a sharply focused laser. This method has been developed as a unique technique to measure translational and rotational diffusion coefficients of molecules in solution and in living cells (22–25). Application of this technique to biological systems has brought to light novel aspects of various molecular dynamisms, such as the status of the tubulin complex in kinesin-mediated axonal transport in the squid giant axon (26). However, this method has not been used to

* This work was supported by grants from the Ministry of Education, Science, Sports and Culture of Japan (to I. W.). The costs of publication of this article were defrayed in part by the payment of page charges. This article must therefore be hereby marked "*advertisement*" in accordance with 18 U.S.C. Section 1734 solely to indicate this fact.

‡‡ To whom correspondence should be addressed: Dept. of Cell Science, Institute of Biomedical Sciences, Fukushima Medical University School of Medicine, Fukushima 960-1295 Japan. Tel.: 81-24-547-1663; Fax: 81-24-549-8898; E-mail: iwada@fmu.ac.jp.

[1] The abbreviations used are: ER, endoplasmic reticulum; CFP, cyan fluorescent protein; FCS, fluorescence correlation spectroscopy; FRAP, fluorescence recovery after photobleaching; YFP, yellow fluorescent protein; DOPA, dihydroxyphenylalanine; VSVG, vesicular stomatitis virus glycoprotein.

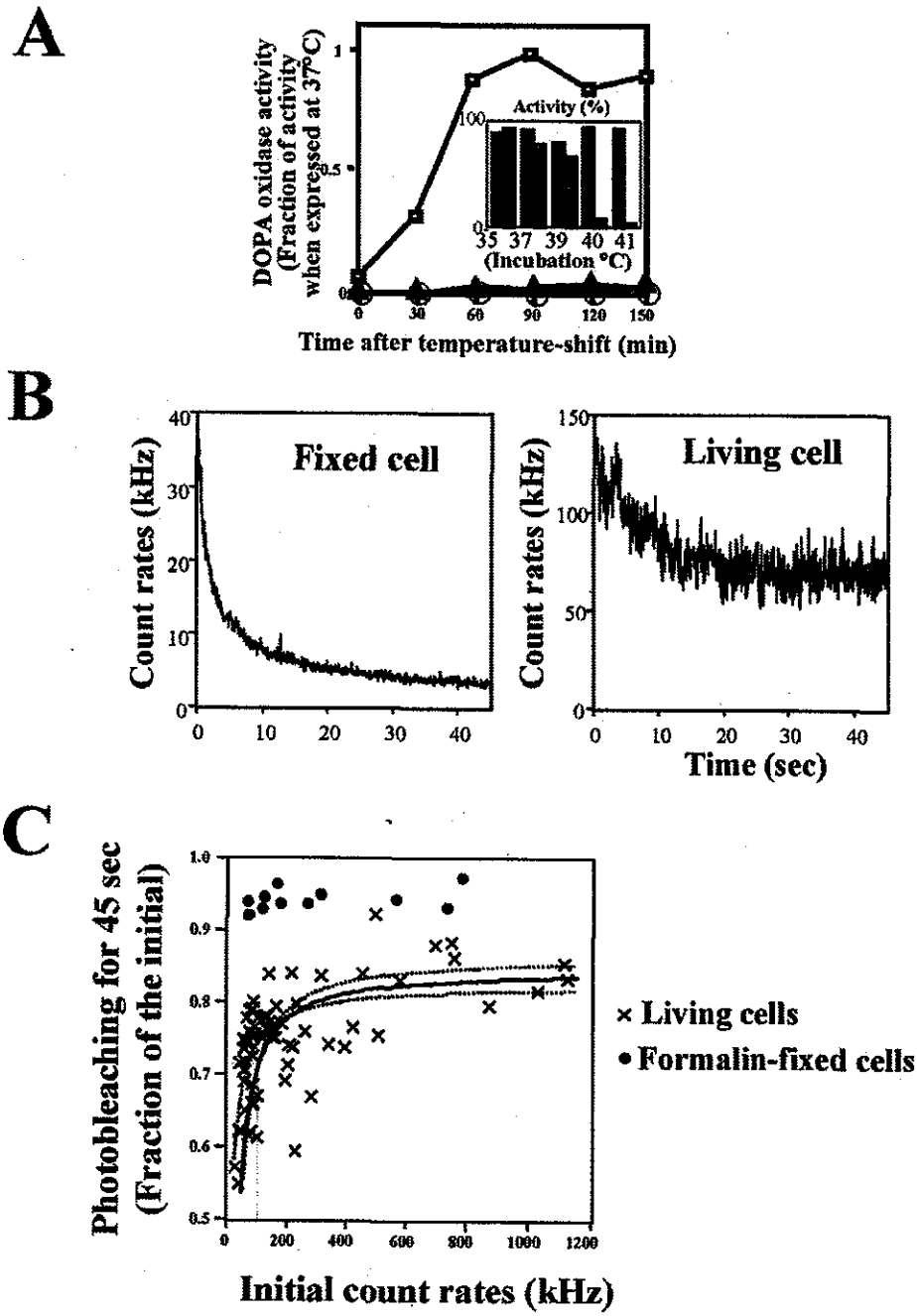

FIG. 1. **Determination of conditions for measuring the diffusional mobility of tyrosinase using FCS.** *A*, thermal synchronization of tyrosinase folding. SiHa cells infected with a recombinant adenovirus expressing wild type tyrosinase were incubated at 40 °C for 24 h and then incubated at 37 °C for the indicated *periods* in the presence of 40 μM puromycin. *Squares*, complete medium; *circles*, ATP-depleted medium; *triangles*, medium with an α-glucosidase inhibitor, castanospermine. *Inset*, *shaded bars*, sensitivity of folding to the culture temperature. Tyrosinase was expressed at the indicated temperatures for 24 h. *Black bars*, stability of mature tyrosinase. Tyrosinase was expressed at 37 °C for 24 h, then incubated at the indicated temperature with 40 μM puromycin for 24 h. The cells were lysed, then the DOPA oxidase activity of the lysates was measured. The amounts of tyrosinase in the lysates were determined by immunoblots. The enzyme activity was expressed as relative activity per immunoreactive tyrosinase. The average of three experiments is shown. *B*, fluorescence intensity (count rate) of tyrosinase-YFP before (*right*) and after (*left*) fixation. An expression vector for tyrosinase-YFP was used to coat beads that were then loaded into COS7 cells and incubated in the presence of brefeldin A (5 μg/ml) for 2 h at 37 °C. The fluorescent signal in a spot in the ER was then counted for 45 s in the living cells (*right*) or recorded in the same medium after fixation with 3.7% formalin for 10 min at 37 °C (*left*). *C*, photobleaching is affected by expression levels. Tyrosinase-YFP was expressed as in *B* and the fluorescence signal of spots in cells was measured. The degree of photobleaching for 45 s was calculated according to the equation: $(I_{ini} - I_{min})/I_{ini}$, where I_{ini} is the initial rate and I_{min} the minimum rate during a 45-s recording period (×, living cells; *dots*, fixed cells). Assuming that the relationship fits with the saturation binding curve, the best-fitting curve was determined using PRISM software. The area of 95% confidence is indicated by the *dotted lines*.

analyze the process of protein maturation in living cells.

To study the dynamics of immature proteins, we reasoned that we might be able to use the thermal sensitivity of tyrosinase, a melanosomal membrane enzyme catalyzing the oxidation of monohydric phenols, a critical step in melanin biosynthesis (EC 1.14.18.1) (27). Failure to express its catalytic

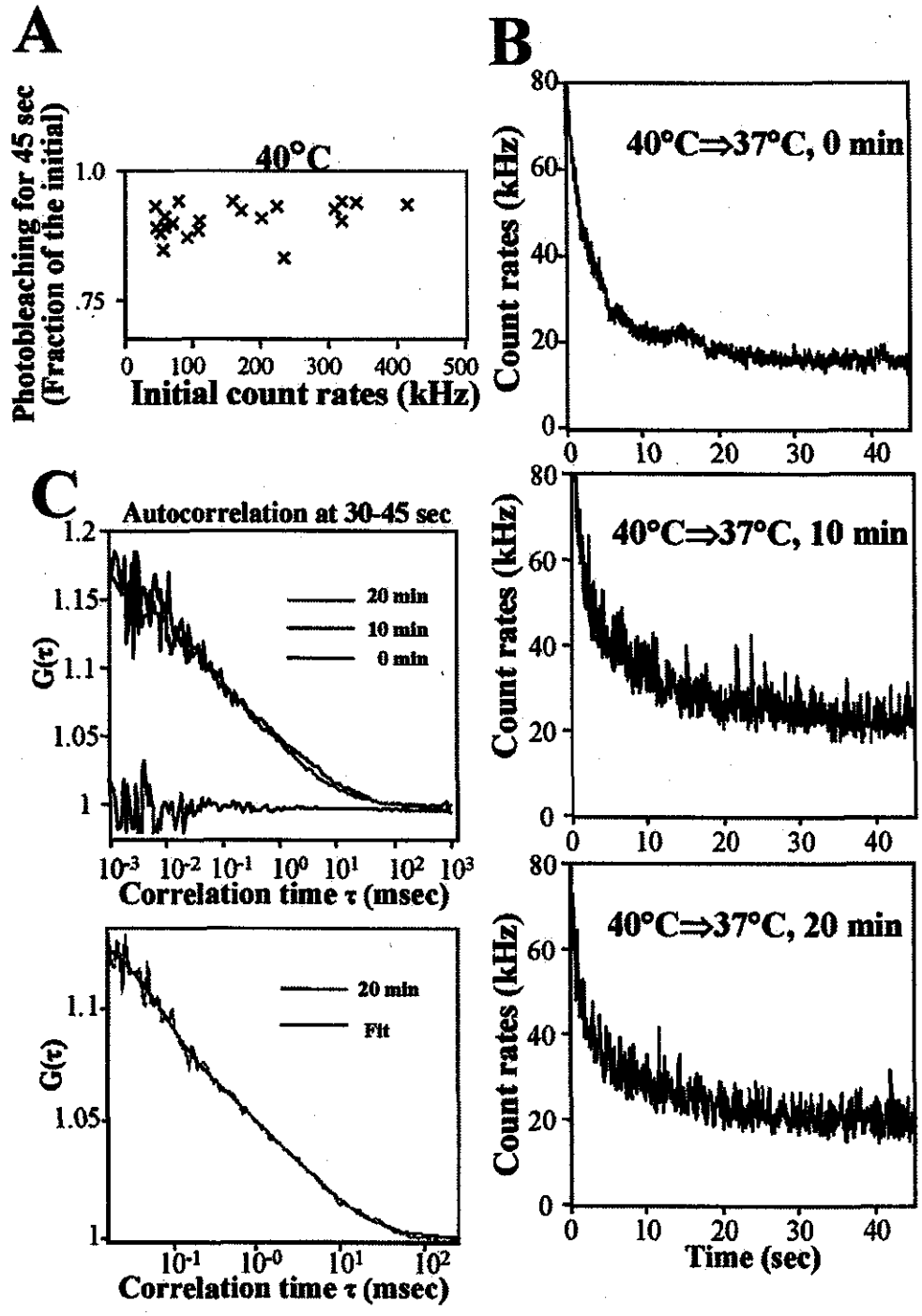

FIG. 2. **FCS measurements of thermally misfolded tyrosinase.** Tyrosinase-YFP was expressed at 40 °C for 2 h and its diffusional motion in the ER was measured by FCS. *A*, photobleaching of thermally misfolded tyrosinase. The photobleached fraction was plotted against the expression levels as in Fig. 1*C*. In this case, the photobleached fraction does not depend on the initial intensity. *B*, changes in fluorescence fluctuation upon temperature shift. Immediately after synthesis at 40 °C for 2 h, fluorescence was recorded in the ER for 45 s (*top*). The same cells were then incubated on the microscopic stage at 37 °C in the presence of 40 μM puromycin and the fluorescence of the same spot was recorded at 10 (*middle*) and 20 min (*bottom*). *C*, autocorrelation function of *B*. Autocorrelation function of the last 15 s of the recording period is shown at 0 (*top panel, black line*), 10 (*green line*), and 20 min (*black line*) after the temperature shift to 37 °C. Thermally misfolded tyrosinase showed little autocorrelation (*top panel, black line*). The best-fit two-component simulation profile (T = 0.64 ms, 50.7% and T = 9.16 ms, 49.3%) of the obtained autocorrelation function data at 20 min is shown in the *bottom panel* (*black line*).

activity results in the occurrence of oculocutaneous albinism type I (28). Pigment cells from individuals with some types of this disorder are temperature-sensitive (29, 30). When wild type tyrosinase is expressed in non-pigmented cells, its folding is also sensitive to heat (31). Completion of tyrosinase folding is a well defined step in that it can be monitored by the acquisition of dihydroxyphenylalanine (DOPA) oxidizing activity either *in situ* or in solution, and it depends entirely on interactions with calnexin (32–35). In non-pigmented cells, tyrosinase is transported to endosomal/lysosomal vesicles (36–40). In this

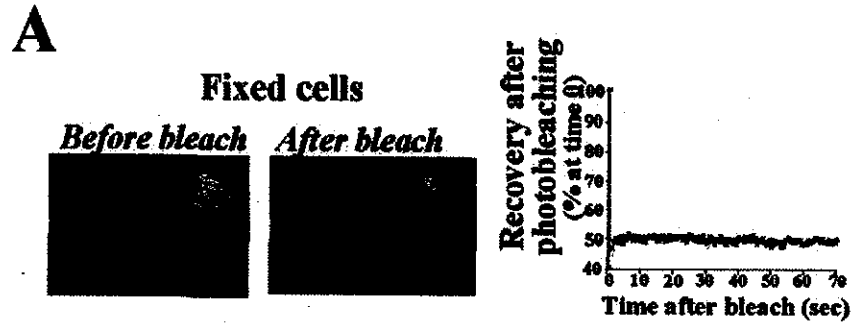

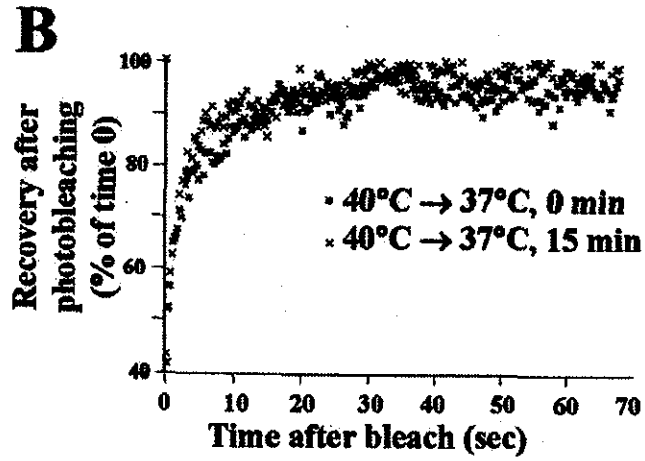

FIG. 3. **FRAP analysis.** Tyrosinase-YFP expression vector was bead loaded onto cells and expressed for 2 h at 40 °C. *A*, FRAP analysis was performed in a formalin-fixed cell. Images of the cell before and after FRAP are shown. The *arrow* indicates a photobleached region. *B*, FRAP analysis of a *living cell*. Recovery rates after photobleaching were measured in an adjacent area of the same single cell at 0 (*red*) or 15 min (*blue*) after a temperature shift to 37 °C in the presence of puromycin. *C*, summary of maximum recovery rates. FRAP was performed in only one region per cell to minimize loss of the mobile fraction by another round of FRAP. *n*, number of measurements.

C

Expression condition	Max recovery (%)
40°C → 37°C 0 min (n=20)	88.8 ± 7.9
40°C → 37°C 15 min (n=20)	90.4 ± 8.3

study we first tested whether the diffusion of folded tyrosinase is measurable. We then studied how the dynamics change in the thermally restricted condition. We also used FRAP to determine the fraction of the population that was immobilized. Our results show that folding appears to be regulated at various levels of microdynamics.

EXPERIMENTAL PROCEDURES

Expression Vectors and Culture Cells—The adenovirus vector used to express tyrosinase is described elsewhere (41). EcoRI and BamHI sites were attached to the human tyrosinase cDNA (35) by polymerase chain reaction (PCR). Tyrosinase fused to yellow fluorescent protein (YFP) or cyan fluorescent protein (CFP) was then produced by ligating the human tyrosinase into pEYFP-N1 or pECFP-N1 (BD Bioscience) cut with EcoRI and BamHI, respectively. For construction of the Sar1(T39N) expression vector, Sar1 cDNA was isolated by reverse transcription from HepG2 RNA using the primer 5′-GGATCAGTCCAGAGAAGTAAAAC-3′, then amplified by PCR with the pair of primers 5′-GCCGGAGAGCCCCTCAGGCCGTAGTAAGC-3′ and 5′-TCACCGTCCAAACATCAGTCAATATACTGG-3′. Restriction sites for BglII and KpnI were created at the 5′ and 3′ ends of the Sar1 cDNA using PCR. The Sar1 cDNA was then ligated into the corresponding sites of pEYFP-N1Δ whose EYFP open reading frame was removed by restriction with BamHI and NotI followed by ligation after polishing the terminus. To construct the GDP-restricted form of Sar1, the codon for Thr at amino acid 36 was mutated to that encoding Asn using the QuikChange™ protocol (Stratagene, La Jolla, CA). An expression vector for CFP-GT-(1–81) (GT-(1–81); the amino-terminal 81 amino acids of human β-1,4-galactosyltransferase) were purchased from Clontech. A vector for VSVG (ts045) was described previously (42). These vectors were introduced directly into cells using siliconized glass microbeads (42). SiHa and COS7 cells were obtained from the American Type Culture Collection (Manassas, VA). COS7 cells stably expressing hSec13-YFP were generated as follows. The coding sequence of human Sec13-YFP (42) was subcloned into the appropriate cloning sites of the retrovirus expression vector, pCX4bsr. pCX4bsr, a generous gift from Dr. T. Akagi (Osaka BioScience Institute), is a modified version of pCXbsr (43) that lacks the internal initiation codons within the gag region. The recombinant retrovirus was generated as described (43) and used to infect COS7 cells. The cells expressing hSec13 were selected by culturing them in Dulbecco's modified Eagle's medium containing blasticidin (10 μg/ml).

Analysis of Protein Dynamics in Living Cells—Live cell analysis using the microscopy was essentially described previously (42). The culture temperature of cells on the microscope stage was controlled using an objective heater for a planapochromat lens ×63 (Bioptechs, Butler, PA) or a Silicon Heater (Cell MicroControls, Norfolk, VA) for a C-Apochromat ×40 lens in combination with a stage heater (Kitazato Supply, Fujinomiya, Japan). To monitor the temperature of the cells

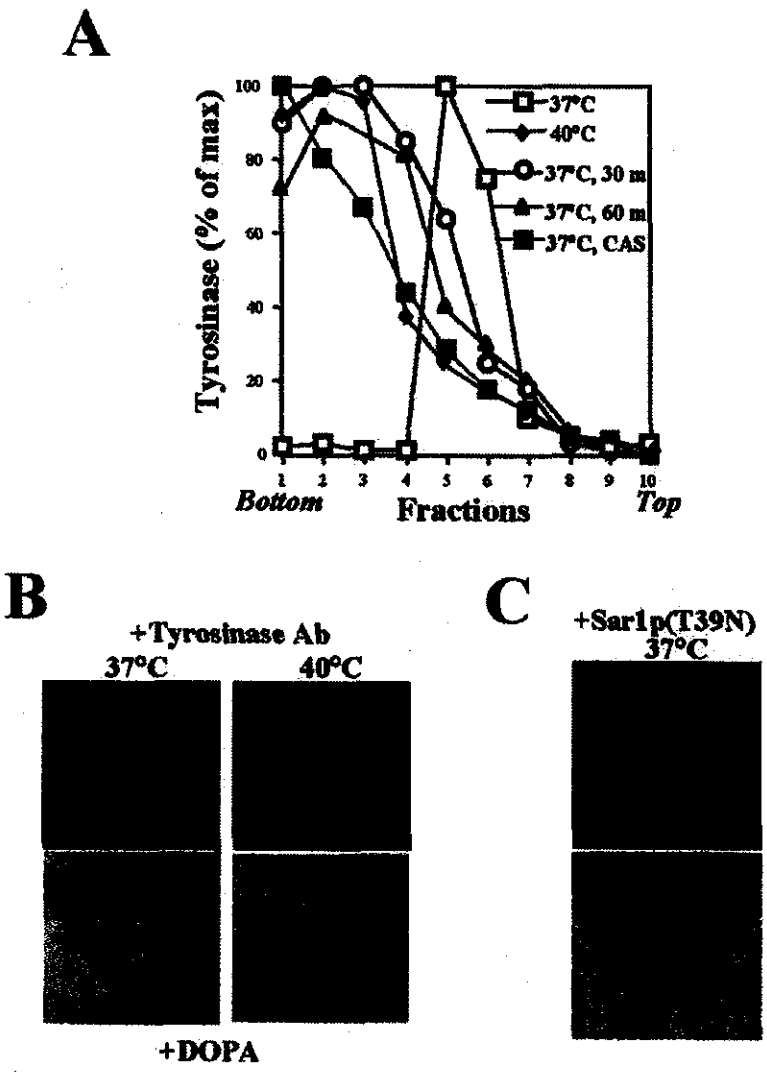

FIG. 4. **Characterization of tyrosinase maturation.** *A*, sedimentation velocity analysis of tyrosinase. Tyrosinase was expressed in SiHa cells at 37 (*black box*) or 40 °C (*other symbols*) for 24 h in the presence (*gray box*) or absence (*other symbols*) of 1 mM castanospermine, and then incubated at 37 °C with puromycin. Cells were lysed and applied to a sucrose gradient of 10–25%. The gradients were centrifuged and the fractions were collected from the bottom of the tube. As molecular mass markers, bovine serum albumin (5 S), catalase (11 S), and apoferritin (17 S) were recovered in fractions 8, 5–7, and 4–5, respectively. See "Experimental Procedures" for details. *B*, active staining of tyrosinase *in situ* at the non-permissive or the permissive temperature. Tyrosinase was expressed in SiHa cells at 37 (*left panels*) or 40 °C (*right panels*) for 24 h using recombinant adenovirus, and stained with anti-tyrosinase antibody (*top panels*) followed by an Alexa 488-labeled anti-mouse antibody or DOPA staining *in situ* (*bottom panels*) as described (35). Fluorescence (*top panels*) and transmission images (*bottom panels*) are shown. *C*, GDP-restricted form of Sar1 inhibits ER export of tyrosinase. The Sar1(T39N) expression vector was co-loaded into COS7 cells with the tyrosinase-YFP expression vector using glass beads. Tyrosinase-YFP fluorescence observed at 3 h post-loading was directly recorded and the active staining pattern was recorded as a transmission image.

under observation, an infrared thermometer (model CT820, CITIZEN Co., Tokyo, Japan) was used. For confocal microscopy and FCS analysis, a ConfoCor2 instrument (Zeiss, Jena, Germany) was used. Confocal images were taken with the laser scanning microscopy module. The excitation light of an argon ion laser at 514 nm was reflected by a dichroic mirror (HFT 514) and focused through a C-Apochromat ×40, NA = 1.2 water immersion objective (pinhole width 70 μm). A 530–560 nm band-pass filter was used to filter out the remaining scattered laser light. In all measurements, the minimum laser power of the setup was used. The fluorescence signal was recorded for three consecutive periods of 15 s (time resolution, 200 ns). The autocorrelation function and data fitting was performed with the software provided with the setup. Indirect immunofluorescence of fixed cells and time-lapse analysis of fluorescent molecules in live cells were carried out and processed as described previously by Nagaya *et al.* (42). For FRAP experiments, an area (1 μm^2) was exposed to the maximum power of the argon laser and then the recovery from the bleaching was measured at the minimum power of the laser. The obtained data were analyzed by fitting to a formula for one-dimensional diffusion (44) using Prism version 3.0 software (San Diego, CA).

Tyrosinase Activity Measurements and Sedimentation Analysis—Active staining of DOPA oxidase and spectrophotomeric measurements of DOPA oxidase activity in cellular lysates were carried out as described (35). To determine the sedimentation velocity of tyrosinase synthesized under various culture conditions, cells in a 60-mm dish were lysed with 0.5 ml of 1% sodium cholate, 0.15 M NaCl, 20 mM potassium phosphate, pH 7.2, and directly loaded onto a sucrose gradient from 25 to 10% in 0.3% sodium cholate, 0.15 M NaCl, 20 mM potassium phosphate, pH 7.2, in a tube for a Hitachi RPS40T rotor. After centrifugation at 36,000 rpm for 18 h at 4 °C, ten 1-ml fractions were collected from the bottom of the tube and 10 μl from each fraction was subjected to immunoblot analysis using an anti-tyrosinase monoclonal antibody (Novocastra Laboratories Ltd., Balliol Business Park West, UK).

RESULTS

FCS Measurements of Tyrosinase Expressed in Non-pigmented Cells—To test whether we could use the reported thermal sensitivity of tyrosinase folding to synchronize its maturation, we first examined the heat lability of its folding and stability. A recombinant adenovirus was used to express tyrosinase in human cervical carcinoma SiHa cells for 24 h at 37 °C and at various other temperatures (Fig. 1*A*). For the cells incubated at 37 °C, protein synthesis was halted by the addition of puromycin and the cells were further incubated for 24 h at the indicated temperatures. The cells were then lysed with detergents and the DOPA oxidase activity was determined (35). The DOPA oxidase activity was dramatically reduced when tyrosinase was synthesized above 39 °C (Fig. 1*A*, *inset*). In contrast, thermal treatment of folded tyrosinase (*i.e.* tyrosinase synthesized at 37 °C) had little effects on the activity, indicating that completion of tyrosinase folding is arrested above 39 °C. Importantly, when the inactive tyrosinase formed at 40 °C was further incubated at 37 °C in the presence of puromycin, the protein became almost fully active with 60 min (Fig. 1*A*, *squares*). This activation was not observed in ATP-depleted medium (*circles*) or in the presence of an α-glucosidase inhibitor (*triangles*).

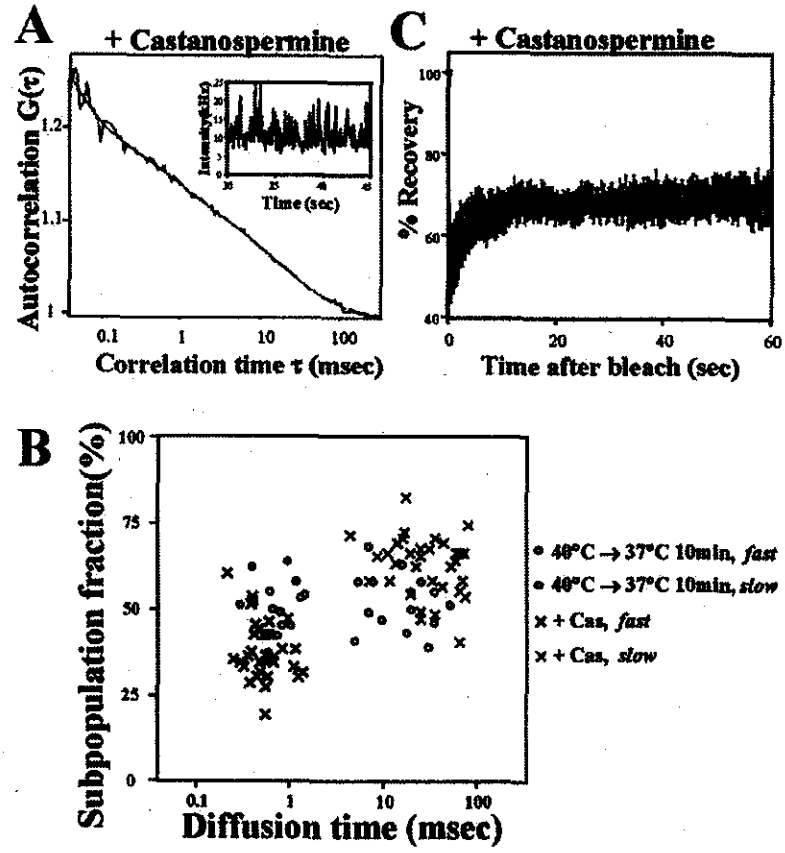

FIG. 5. **FCS and FRAP analysis of tyrosinase-YFP in castanospermine-treated cells.** Misfolded tyrosinase-YFP expressed in the presence of castanospermine at 37 °C for 2 h was subjected to FCS (*A*) or FRAP (*C*) analysis as described in the legends to Figs. 2 and 3, respectively. *Panel A*, best fitting two-component simulation profile (T = 0.59 ms, 45.6%, and T = 18.7 ms, 54.4%) (*black line*) and the autocorrelation function data (*blue line*). *Inset*, fluorescence fluctuation (the last 15 s of the recording period of three consecutive recordings) used for the autocorrelation analysis. *Panel B*, summary of FCS measurements. In the *upper panels*, fast and slow diffusion time in cells treated as indicated are plotted against the percentage of subpopulation estimated as in *panel A*. Averaged values and S.E. at each condition were calculated and are shown in the table. *N.D.*, not determined because of lack of autocorrelation. *Panel C*, recovery rates after photobleaching. The *error bars* are the measured S.E. (n = 6).

Expression condition	Diffusion time (msec) / (%) *Fast*	*Slow*
40°C (n=15)	N. D.	N. D.
40°C → 37°C 10 min (n=15)	0.768 ± 0.315 / (49.7 ± 7.6)	26.9 ± 16.7 / (41.7 ± 8.4)
+ CAS (n=33)	0.575 ± 0.275 / (37.8 ± 8.5)	46.1 ± 29.2 / (62.3 ± 8.6)

We then used this protocol to study how the mobility of tyrosinase is regulated during maturation. We reasoned that the diffusion profile of thermally misfolded tyrosinase may be distinct from the properly folded molecule if there is any regulation of mobility. To analyze mobility, we used FCS because this technique has the highest time resolution of the available techniques. However, it is known that FCS is often too sensitive to analyze cellular processes (21). In particular, photobleaching is a major obstacle. We therefore examined the conditions in which FCS could detect random diffusion in living cells. Because the degree of photobleaching obtained by FCS should correlate with the density of the molecules, we investigated which expression level would largely allow for random diffusion. In cells where the expression level is too high, the molecules would be at least partially immobilized. To achieve various levels of expression, we used siliconized glass microbeads (42). When photon-counting of tyrosinase-YFP was carried out in formalin-fixed cells, all fluorophores showed rapid decay of fluorescence to near background within 45 s, as expected (Fig. 1*B*, *left panel*). The fluctuation of the signal was almost at the level of noise, and no autocorrelation was observed from this counting (not shown). We next examined whether this setup could detect diffusion of tyrosinase-YFP expressed in a living cell at 37 °C for 2 h in the presence of brefeldin A, which prevents export from the ER (45). In this measurement, the degree of photobleaching was reduced compared with that in the fixed cells, and massive signal fluctuation was observed (Fig. 1*B*, *right panel*).

When we plotted the extent of bleaching, B, against the expression level, I_{ini}, we noticed that the relationship largely fits a simple saturable binding model: $B = B_{max} \cdot I_{ini}/(K + I_{ini})$. The constant K reflects the degree of correlation between photobleaching and the expression level. In the case of fixed cells, K should be ~0. If the level of tyrosinase expression has little influence on diffusional motion in the membrane, K should far exceed I_{ini}. This would happen if the fluorophore is very bright, so that the number of expressed molecules is very small. However, when measured in the living cells, this is not the case. In the living cells, a significant correlation was observed between the two values when the initial count rate was below 100 kHz (Fig. 1*C*, ×), suggesting that at least tyrosinase-YFP was not saturated at this range and, thus, random diffusion of tyrosinase-YFP should be measurable.

Regulation of Diffusional Mobility of Thermally Misfolded Tyrosinase—We next expressed tyrosinase-YFP at 40 °C and plotted the degree of photobleaching against the number of misfolded molecules. Surprisingly, massive photobleaching was observed irrespective of the expression level (Fig. 2*A*). A typical decay curve is shown in Fig. 2*B* (*top panel*), which resembles that of the fixed protein (Fig. 1*B*). It should be noted

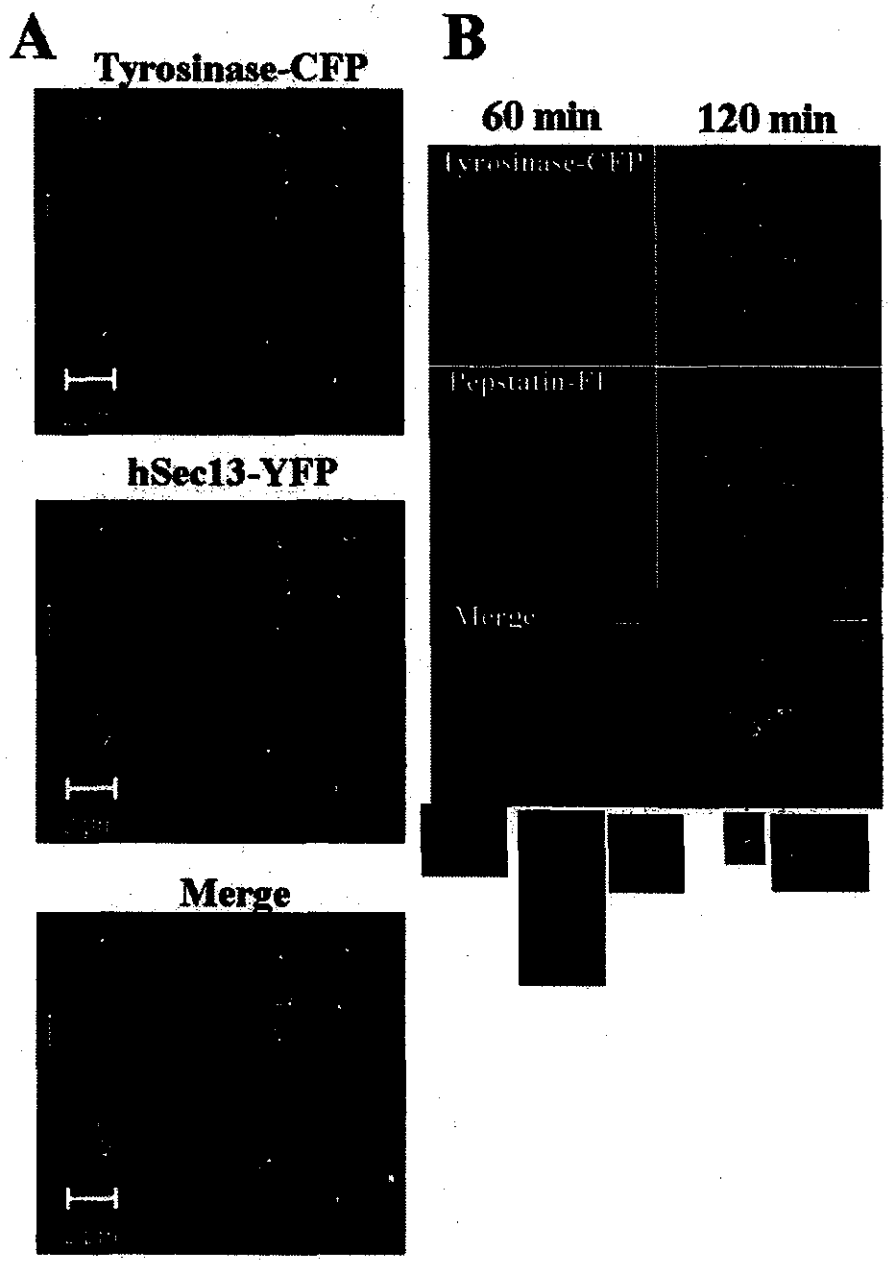

FIG. 6. **Targeting of tyrosinase-CFP in COS7 cells.** *A*, tyrosinase-CFP was concentrated in COPII-coated structures. Tyrosinase-CFP was expressed at 40 °C for 2 h in COS7 cells stably expressing hSec13-YFP. After the addition of puromycin, the cells were placed on a microscope stage and incubated at 37 °C. Shown are images in the ER network at 4 min. Most punctate structures containing tyrosinase-CFP (*red*) were coated with hSec13-YFP (*green, white arrows*). *B*, targeting of tyrosinase to lysosomes. Tyrosinase-CFP (*red*) was expressed as in *A* and incubated at 20 °C for 2 h in the presence of BODYPY-FL-labeled pepstatin (25 ng/ml, *green*) and puromycin. The medium was then changed to fresh medium without the labeled pepstatin and incubated for 1 or 2 h at 37 °C. At 1 h, most tyrosinase-containing structures were found in structures adjacent to pepstatin-positive vesicles, as shown in the enlarged images in the 60-min column. After incubation for another hour, most of the tyrosinase signals became completely merged with the fluorescent pepstatin signals, as shown in the enlarged images in the 120-min column.

that, different from the fixed cells, the decay in living cells reached a plateau at a significantly higher level than background (~1 kHz), suggesting the presence of a slow movement of nonbleached tyrosinase into the bleached area. However, this mobility was too slow to be captured by FCS. Nonetheless, the counting showed almost no autocorrelation over time (Fig. 2*C*, *black line*). To know if this lack of fluctuation is reversed when folding is allowed, we recorded the fluorescence in the same spot over a temperature shift from 40 °C (Fig. 2*B*, *top*) to 37 °C (Fig. 2*B*, *middle* and *bottom*). In these cases, fluctuation emerged upon temperature shift (Fig. 2*B*, *middle*). Interestingly, an almost identical autocorrelation curve was observed when incubation was continued at 37 °C for another 10 min (Fig. 2*C*, *red line*), except for a slight increase in the population with the faster mobility in the millisecond range. A two-component fitting analysis indicated that the mobility was composed of fast (T = 0.64 ms, 50.7%) and slow (T = 9.17 ms, 49.3%) diffusion components (Fig. 2*C*, *bottom panel*).

While these results indicated that the random diffusion detected by FCS was suppressed at 40 °C, they also suggested that the protein was slowly mobile at this temperature. We therefore examined whether such dynamics might be detected by FRAP. To test this possibility, we first assayed the rates of reversible photobleaching in fixed cells (46). An area of a formalin-fixed tyrosinase-YFP was photobleached by a pulse of intense laser beam, and the recovery rate was determined. As shown in Fig. 3*A*, the maximum laser beam reduced the signal to 42% of the initial level and within 1 s the intensity increased to 50% and remained there, suggesting that any recovery above 50% should be because of fluorophore exchange between the bleached and unbleached areas. We then determined the fraction of immobilized molecules in the living cells. While the fluorescence intensity of an area of tyrosinase-YFP synthesized for 2 h at 40 °C was reduced almost as much as it was in the fixed cell by an intense laser beam, the signal in the area recovered almost fully (Fig. 3*B*, *red*). Similarly, full recovery

from photobleaching was observed in the adjacent area when the cell was incubated on the stage at 37 °C for 15 min after 40 °C expression for 2 h although it appeared to be slightly faster (Fig. 3*B*, *blue*). These results and further independent experiments, as summarized in Fig. 3*C*, indicates that tyrosinase synthesized at 40 °C was slow, but fully mobile.

Diffusional Mobility of Aggregated Tyrosinase Formed in Castanospermine-treated Cells—To know whether the apparent lack of random diffusion seen with FCS measurements at non-permissive temperatures was because of the formation of large aggregates, we measured the molecular weight of detergent-solubilized tyrosinase using sedimentation analysis through sucrose density gradients. As shown in Fig. 4*A*, tyrosinase synthesized at the non-permissive temperature, 40 °C, was mostly found in the bottom three fractions of the gradient (*red line*). After 30 min at 37 °C, the majority was still found in the bottom fractions, but a slight increase in the recovery in fractions 4 and 5 was observed (*green line*). After 1 h at 37 °C, a small decrease in the percentage of tyrosinase in the bottom fraction was detected (*blue line*). An almost identical pattern was obtained at 2 h postincubation.[2] However, the molecules did not acquire the compact tertiary structure detected for the native enzyme synthesized without exposure to 40 °C (*black line*). When we examined terminally misfolded tyrosinase synthesized in the presence of an α-glucosidase inhibitor, castanospermine, the majority of the molecules were recovered in the bottom fractions, suggesting that they are largely aggregated. This analysis suggests that a slight alteration in size of tyrosinase aggregates is associated with the acquisition of activity, and that the thermally misfolded tyrosinase is structurally distinct from terminally misfolded tyrosinase.

To examine the possibility that the suppression of millisecond diffusion at the non-permissive temperature was caused by enhanced aggregation, we measured diffusion of the terminally misfolded tyrosinase synthesized in castanospermine-treated cells at 37 °C. However, in this case, the autocorrelation analysis showed that the diffusion of the slower mobility component was slightly slower but detectable by FCS (Fig. 5*A*). The typical measurement showed that the diffusion was composed of a fast (586.8 μs, 45.6%) and a slow (18.7 ms, 54.4%) diffusion (Fig. 5*A*). A summary of FCS measurements at various conditions is also shown in Fig. 5*B*. Hence, we conclude that the lack of autocorrelation at the non-permissive temperature was not the result of enlarged aggregates. However, FRAP analysis of the castanospermine-treated cells showed that the maximum recovery rate was reduced by ~30% (Fig. 5*C*). Taken together, we reasoned that long range diffusion, which is not observed in triglucosylated tyrosinase, is directly associated with the acquisition of the enzyme activity.

Enzymatically Active but Non-native Tyrosinase Was Transported to Lysosomes—Finally, we studied the fate of tyrosinase after a temperature shift to investigate whether the non-native but fully diffusible tyrosinase is properly targeted to lysosomes. The thermally misfolded tyrosinase was confined in the ER as expected (Fig. 4*B*). When a GDP-restricted form of Sar1, whose expression inhibits export of cargo from the COPII-coated ER exit sites, was co-expressed with tyrosinase at 37 °C, tyrosinase was retained in the ER and DOPA oxidase activity was expressed (Fig. 4*C*). Indeed, at 4 min after the temperature shift, at least some tyrosinase appeared to be concentrated in hSec13-coated structures (Fig. 6*A*). As shown in Fig. 7, time-lapse analysis revealed that transport to the Golgi apparatus, which was demarcated by coexpression of the Golgi marker

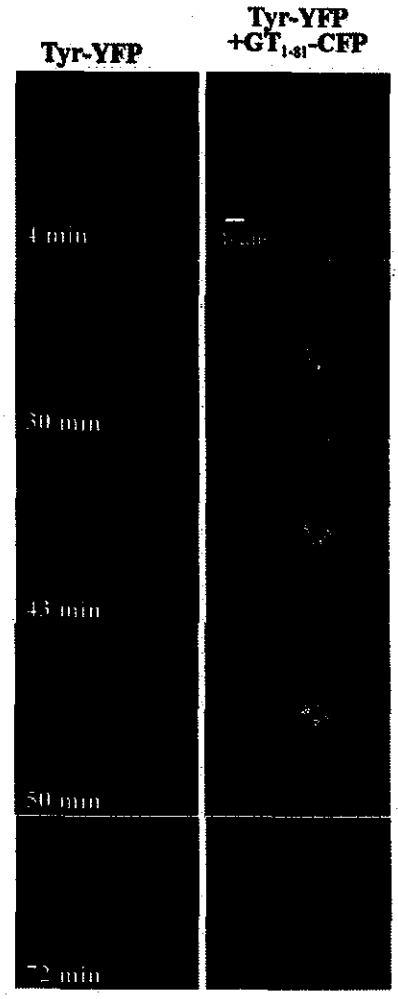

FIG. 7. **Transport of tyrosinase to lysosomes in a single cell.** Expression vectors for tyrosinase-YFP and CFP-GT-(1–81) were introduced into COS7 cells by siliconized glass microbeads and incubated for 2 h at 40 °C. The temperature was lowered to 37 °C after the addition of 40 μM puromycin and then both fluorescent images were recorded at *20-s intervals*. The *green* images represent tyrosinase-YFP and the *red* images represent CFP-GT-(1–81) in the same cell.

galactosyltransferase-(1–81)-CFP, was clearly observed at 30 min after a temperature shift from 40 to 37 °C (Fig. 7, *red*). Further incubation allowed the initial formation of small vesicles at 50 min and of large granules at 72 min. The larger granules were identified as lysosomes because tyrosinase colocalized with lgp85 within them.[2] Interestingly, tyrosinase was found in compartments adjacent to lysosomes before merging with pepstatin-positive lysosomes (Fig. 6*B*, *bottom*). Thus, acquisition of enzyme activity and proper targeting to lysosomes in a classical pathway appears to occur only when diffusion in the millisecond range and slow but full exchange in the ER are allowed during maturation in the ER.

DISCUSSION

The dynamics of proteins in living cells are regulated at various levels. Folding depends on the molecules' "breathing," that is, on fluctuations in the relative positions of amino acid residues, but excessive collisions may lead to nonproductive interactions. We therefore reasoned that diffusion should be regulated upon maturation. To examine this process in living cells, it is necessary to manipulate the status of folding. The ts045 strain of VSVG (47) was the only well characterized cargo

[2] A. Kamada, H. Nagaya, T. Tamura, M. Kinjo, H.-Y. Jin, T. Yamashita, K. Jimbow, H. Kanoh, and I. Wada, unpublished data.